

# Neutral atomic-carbon QSO absorption-line systems at $z > 1.5$ : Sample selection, H I content, reddening, and 2175 Å extinction feature\*

C. Ledoux<sup>1</sup>, P. Noterdaeme<sup>2</sup>, P. Petitjean<sup>2</sup>, and R. Srianand<sup>3</sup>

<sup>1</sup> European Southern Observatory, Alonso de Córdova 3107, Casilla 19001, Vitacura, Santiago 19, Chile  
e-mail: cledoux@eso.org

<sup>2</sup> Institut d'Astrophysique de Paris, CNRS and UPMC Paris 6, UMR 7095, 98bis boulevard Arago, 75014 Paris, France

<sup>3</sup> Inter-University Centre for Astronomy and Astrophysics, Post Bag 4, Ganeshkhind, 411 007 Pune, India

Accepted for publication 20 April 2015

## ABSTRACT

We present the results of a search for cold gas at high redshift along QSO lines-of-sight carried out without any a priori assumption on the neutral atomic-hydrogen content of the absorbers. To do this, we systematically looked for neutral-carbon (C I)  $\lambda\lambda 1560, 1656$  transition lines in 41 696 low-resolution QSO spectra ( $1.5 < z_{\text{em}} < 4.46$ ) from the SDSS-II - Data Release seven - database. C I absorption lines should indeed probe the shielded gas in the neutral interstellar medium of galaxies more efficiently than traditional tracers such as neutral atomic-hydrogen (H I) Damped Lyman- $\alpha$  (DLA) and/or Mg II systems.

We built up a sample of 66 C I absorbers with redshifts in the range  $1.5 < z < 3.1$  and rest-frame equivalent widths  $0.1 < W_r(\lambda 1560) < 1.7$  Å. The completeness limit of our survey is  $W_{r,\text{lim}}(\lambda 1560) \approx 0.4$  Å. C I systems stronger than that are more than one hundred-times rarer than DLAs at  $z_{\text{abs}} = 2.5$ . The number of C I systems per unit redshift is found to increase significantly below  $z = 2$ . We suggest that the C I absorbers are closely related to the process of star formation and the production of dust in galaxies and that their cosmic evolution is driven by the interplay between dust shielding and the evolution of the ultra-violet background at  $\sim 10$  eV.

We derive the neutral atomic-hydrogen content of the C I systems observable from the southern hemisphere from VLT/UVES spectroscopy and find that a majority of them are sub-DLAs with  $N(\text{H I}) \sim 10^{20}$  atoms  $\text{cm}^{-2}$ . The dust content of these absorbers is yet significant as seen from the redder optical colours of the corresponding background QSOs and their reddened spectral energy distributions, with  $E(B-V)$  values up to  $\sim 0.3$ . The overall  $N(\text{H I})$  distribution of C I systems is relatively flat however. As a consequence, among the C I systems classifying as DLAs there is a probable excess of strong DLAs with  $\log N(\text{H I}) > 21$  (atoms  $\text{cm}^{-2}$ ) compared to systematic DLA surveys. While the dust content of such systems is significant, their dust-to-gas ratio must still be limited. Indeed, strong DLAs having large amounts of shielded gas and dust producing stronger reddening and extinction of the background QSOs if they exist should have been missed in the current magnitude-limited QSO sample.

We study empirical relations between  $W_r(\text{C I})$ ,  $N(\text{H I})$ ,  $E(B-V)$  and the strength of the 2175 Å extinction feature, the latter being detected in about 30% of the C I absorbers. We show that the 2175 Å feature is weak compared to Galactic lines-of-sight exhibiting the same amount of reddening. This is probably the consequence of current or past star formation in the vicinity of the C I systems. We also find that the strongest C I systems tend to have the largest amounts of dust and that the metallicity of the gas and its molecular fraction is likely to be high in a large number of cases. The C I-absorber sample presented here hence provides ideal targets for detailed studies of the dust composition and molecular species at high redshift.

**Key words.** cosmology: observations – quasars: absorption lines – galaxies: ISM – dust, extinction

## 1. Introduction

Understanding the mechanisms of star formation at high redshifts is central to our knowledge of how galaxies formed and subsequently evolved chemically. This is specially true at  $z \sim 2$  when the cosmic star-formation activity was highest (Madau & Dickinson 2014). Stars form out of cold gas, metals and dust in molecular clouds (e.g. Snow & McCall 2006) in the interstellar medium (ISM) of galaxies. In turn, the radiative and mechanical feedbacks from stars have a strong impact on the physical state of the ISM. Studying the ISM at high redshifts, and in particular deriving the physical properties of the diffuse

molecular phase in galaxies, is therefore crucial for understanding how stars formed in the early Universe.

The best way to derive physical properties accurately is to detect the tracers of the cold gas in absorption (see Muller et al. 2014). The neutral, shielded and possibly cold gas clouds at high redshifts can be searched for in the radio domain by targeting the neutral atomic-hydrogen (H I) 21-cm absorption line (e.g., Gupta et al. 2009). However, systematic - blind - surveys have to await the increased sensitivity of new facilities such as MeerKAT/SKA and ASKAP (Booth et al. 2009; Duffy et al. 2012). On the other hand, such a gas can be efficiently traced in the optical wave-bands by detecting the redshifted H I damped Lyman- $\alpha$  (Prochaska et al. 2005; Noterdaeme et al. 2009b, 2012) and/or strong Mg II (e.g., Quider et al. 2011; Budzynski & Hewett 2011) lines imprinted in the spectra of bright enough background sources such as QSOs or the rapidly fading  $\gamma$ -ray burst (GRB) afterglows (for the latter, see Fynbo et al. 2009, and references therein).

\* Based on data from the Sloan Digital Sky Survey (SDSS) and dedicated follow-up observations carried out at the European Southern Observatory (ESO) under programmes 082.A-0544 and 083.A-0454 (P.I. Ledoux) using the Ultra-violet and Visual Echelle Spectrograph (UVES) installed at the Nasmyth-B focus of the Very Large Telescope (VLT), Unit-2 (Kueyen), on Cerro Paranal, Chile.

Damped Lyman- $\alpha$  systems (hereafter DLAs) observed in QSO spectra have column densities of  $N(\text{H I}) \geq 2 \times 10^{20}$  atoms  $\text{cm}^{-2}$  and are known to contain most of the neutral gas in the Universe in the redshift range  $0 < z < 5$  (see Wolfe et al. 2005, for a review). It has been shown however that DLAs typically probe warm ( $T \gtrsim 3000$  K) and diffuse ( $n_{\text{H}} < 1 \text{ cm}^{-3}$ ) neutral gas (e.g., Petitjean et al. 2000; Srianand et al. 2012). The metallicity of DLAs is generically low, i.e., on an average about 1/30<sup>th</sup> of Solar (Pettini 2006; Rafelski et al. 2012) and their dust-to-gas ratio is typically less than one-tenth of what is observed in the Galactic ISM (e.g., Vladilo et al. 2008). This probably explains the low detection rates of molecular hydrogen ( $\text{H}_2$ ) in DLAs where only about 10% of the QSO lines-of-sight intercept  $\text{H}_2$ -bearing gas down to a limit of  $N(\text{H}_2) \sim 10^{14}$  molecules  $\text{cm}^{-2}$  (e.g., Noterdaeme et al. 2008a; Balashev et al. 2014; for searches for  $\text{H}_2$  in DLAs originating from the host galaxies of GRBs, see Ledoux et al. 2009; Krühler et al. 2013).

Based on the observed correlation between metallicity and dust depletion in DLAs (Ledoux et al. 2003), DLAs with high metallicity are expected to contain more dust and therefore to exhibit larger  $\text{H}_2$  fractions (see Petitjean et al. 2006). However, even in DLAs with the highest metallicities typical dust signatures like reddening of the background QSOs, the 2175 Å extinction feature (hereafter also called ultra-violet [UV] bump), or diffuse interstellar bands, are not apparent. Even in the rare cases with  $\text{H}_2$  detections, the inferred molecular fractions are low and typical of what is seen in Galactic diffuse atomic gas with  $f(\text{H}_2) \equiv 2N(\text{H}_2)/[2N(\text{H}_2) + N(\text{H I})] \lesssim 0.01$  and often much lower than this (see Noterdaeme et al. 2008a). The primary reason for this is that the cold and dusty phases are missed probably because of their reduced cross-sections relative to that of the more pervasive warm neutral ISM (Zwaan & Prochaska 2006). Direct evidence for the relatively small physical sizes ( $\lesssim 0.15$  pc) of  $\text{H}_2$ -detected clouds in DLAs recently came from the observation of partial coverage of the QSO broad-line emitting region (Balashev et al. 2011; Klimentko et al. 2015).

$\text{H}_2$ -detected clouds in DLAs are found to have kinetic temperatures in the range  $T \sim 70 - 200$  K and particle densities  $n_{\text{H}} \sim 1 - 100 \text{ cm}^{-3}$  (e.g., Srianand et al. 2005). When detected,  $\text{H}_2$  is usually coincident with neutral atomic carbon (C I; see also Ge & Bechtold 1999). This is due to the fact that the ionization potential of neutral carbon (11.26 eV) is similar to the average energy of the Lyman-Werner photons that dissociate  $\text{H}_2$ . Therefore, shielding of UV photons is essential for these species to remain at detectable levels. Carbon monoxide (CO) has long escaped detection even in DLAs with detected  $\text{H}_2$ , down to  $N(\text{CO}) \sim 10^{12}$  molecules  $\text{cm}^{-2}$  (see, e.g., Petitjean et al. 2002). This is not surprising since CO, with a dissociation energy of 11.09 eV, needs to be even more shielded than  $\text{H}_2$  and C I to be detected. After CO UV absorption bands were detected for the first time at high redshift, in a sub-DLA towards the QSO SDSS J 143912.05+111740.6 (Srianand et al. 2008b), it became clear that the best place to detect CO in absorption at high redshift are the systems with strong C I absorption. Following this strategy allowed us to detect carbon monoxide subsequently in five additional systems (Noterdaeme et al. 2009a, 2010a, 2011).

In Galactic translucent interstellar clouds, CO starts to be produced in significant amounts when neutral atomic carbon becomes the dominant carbon species and a large fraction of hydrogen turns molecular (Snow & McCall 2006). The strength of the C I absorption is expected to be such that it could be detected even in a low resolution spectrum. We therefore embarked on a systematic search for C I absorption in QSO spectra from the SDSS-II - Data Release seven (hereafter DR 7) - database. In

this paper, we present the results of this search and the basic properties of the detected C I absorbers. Note that here we will equally refer to QSO absorption-line systems detected through C I absorption as “C I systems” or “C I absorbers”.

In Sect. 2, we describe our selection and identification of C I absorbers. We discuss the properties of the sample in terms of intervening C I-absorber number per unit redshift, proximate systems, and C I rest-frame equivalent widths, in Sects. 3.3, 3.4 and 3.1, respectively. We then assess the impact of the C I absorbers on their respective background QSOs both from the observed QSO optical colours (Sect. 4.1) and the reddening these systems induce on the QSO spectral energy distributions (Sect. 4.2). In Sect. 5, we present the H I column-density distribution of the C I systems from VLT/UVES spectroscopy. In Sect. 6, we investigate empirical relations between neutral atomic-carbon and neutral atomic-hydrogen contents, QSO reddening and the strength of possible 2175 Å extinction features (whose measurements are described in Sect. 4.3). We summarise our findings and conclude in Sect. 7.

Throughout this paper, we assume a standard  $\Lambda$  cold dark-matter cosmology with  $H_0 = 70 \text{ km s}^{-1} \text{ Mpc}^{-1}$ ,  $\Omega_{\Lambda} = 0.7$  and  $\Omega_{\text{M}} = 0.3$ .

## 2. C I absorption-line selection and identification

We systematically searched for C I absorption lines in high-redshift QSO spectra from the Sloan Digital Sky Survey (York et al. 2000) – DR 7 (Abazajian et al. 2009) – quasar catalogue (Schneider et al. 2010). This survey imposed an i-band magnitude cut of 19.1 for QSO candidates whose colours indicate a probable redshift smaller than  $\sim 3$ . The spectra cover the wavelength range 3800–9200 Å at a resolving power  $R \sim 2000$ .

We implemented a dedicated IDL procedure to detect and identify absorption-line features in SDSS QSO spectra automatically. Since SDSS spectra are log-lambda binned, the pixels have constant velocity size ( $\approx 69 \text{ km s}^{-1}$ ). This makes it straightforward to cross-correlate the spectra with an emission- or absorption-line template. We used the method introduced by Noterdaeme et al. (2010b) to search for [O III]  $\lambda\lambda 4959, 5007$  emission and Mg II absorption lines. We first normalized the spectra iteratively using Savitzky-Golay filtering. This consists of smoothing the spectra by convolving them with a Savitzky-Golay kernel that preserves the sharp QSO emission-line peaks but ignores narrow features such as metal absorption lines, bad CCD pixels and sky emission-line residuals. Deviant pixels and their neighbours are then masked out and the resulting data is convolved again in the same way, and so on and so forth. This procedure has the major advantage as no *a priori* assumption is required about the functional form of the QSO continuum (i.e., power law or other) and in addition it is computationally extremely fast. We then cross-correlated the normalised spectra with a synthetic profile of C I  $\lambda\lambda 1560, 1656$  absorption lines. We looked for the positive correlation signal together with peak absorptions detected at more than  $2\sigma$  and  $2.5\sigma$ , respectively, and differing by less than a factor of three. The simultaneous detections of the Si II  $\lambda 1526$  and Al II  $\lambda 1670$  absorption lines were required to support the identifications of the two features as C I and hence minimize the probability of chance coincidence. Spurious detections ( $\sim 50\%$ ), most of them close to the detection limit, were identified visually and removed from the sample. In total, we find 66 systems, one of which is shown in Fig. 1.

The search for C I lines was limited to the regions of the spectra redwards of the QSO Lyman- $\alpha$  emission line to avoid the

spurious coincidences that are frequent in the Lyman- $\alpha$  forest. The wavelength range above 7200 Å was also not considered in the search to avoid regions of the spectra heavily affected by residuals resulting from the sky emission-line subtraction. We requested that the search window encompasses the wavelengths of the Si II  $\lambda 1526$  and Al II  $\lambda 1670$  absorption lines of the putative C I systems so that the validity of a system does not rely solely on the detection of two transitions (see above). For a given line-of-sight, the redshift lower bound ( $z_{\min}$ ) of the C I search is therefore the largest value between  $z = 3820/1526 - 1 \simeq 1.50$  and  $(1 + z_{\text{em}}) \times 1215/1526 - 1 \simeq 0.8 \times z_{\text{em}} - 0.2$ , where  $z_{\text{em}}$  is the QSO emission redshift. The redshift upper bound ( $z_{\max}$ ) of the search is the smallest value between  $z_{\text{em}} + 0.1$  (to not exclude a priori proximate systems with infalling velocities of up to  $+5000 \text{ km s}^{-1}$ ) and  $z = 7200/1656 - 1 \simeq 3.35$ . In order to avoid too many false positives at low signal-to-noise (S/N) ratio, we requested the median S/N ratio per pixel to be larger than four for a given spectrum to be actually scanned. This resulted in a sample of 41 696 QSOs with  $1.5 < z_{\text{em}} < 4.46$  whose spectra were searched for intervening or proximate C I absorbers. Note that we did not initially reject Broad Absorption-Line (BAL) quasars because our procedure follows the QSO continuum locally and can detect narrow absorption lines embedded in broad and not fully saturated troughs. Regions of deep absorption are de facto avoided when we study the number of intervening C I absorbers per unit redshift in Sect. 3.3 as they have low S/N ratio per pixel.

Table 1 summarises our C I sample which we refer to in the following as the overall sample. QSO names with J 2000 coordinates are given for each absorber. No line-of-sight is found to feature more than one system<sup>1</sup>. The SDSS plate and fibre numbers as well as the MJD are also provided in the table as useful cross-references. The QSO emission redshifts derived by the SDSS team are indicated together with the absorption redshifts and rest-frame equivalent widths of the C I lines. The latter were carefully determined by us for each individual system. In the next column of the table, we specify the average S/N ratios per pixel in the regions the two C I lines are located. At  $z_{\text{abs}} > 2.2$ , the Lyman- $\alpha$  line of the systems is also covered by the SDSS spectra. We therefore provide in the table a determination of the total neutral atomic-hydrogen column density of these systems following the method developed by Noterdaeme et al. (2009b). The reliability of the latter is confirmed in a number of cases with follow-up high-resolution VLT/UVES spectroscopy (see the last column of Table 1, and Sect. 5). This column also has additional  $N(\text{H I})$  measurements for several low-redshift systems for which Lyman- $\alpha$  absorption is not covered in the SDSS spectrum.

### 3. Sample properties

It must be noted that in this survey C I systems are found without any presumptions on the presence of neutral atomic hydrogen, i.e., the C I systems found in this work do not necessarily have to be DLAs. Moreover, DLA absorbers can be observed in SDSS spectra only when their redshifts are larger than 2.2 while C I lines can be identified down to  $z_{\text{abs}} \simeq 1.50$ . As stated before, the reality of the identified C I systems in our sample was checked by visual inspection. Therefore, we believe the C I detections are secure. We discuss the completeness of the survey in Sect. 3.2.

<sup>1</sup> Note however that there is a second C I system towards SDSS J 234023.67–005327.1, which, with  $z_{\text{abs}} = 1.36$ , falls below the redshift cut-off of our survey. This system happens to be detected in 21-cm absorption hence is also related to cold gas (see Gupta et al. 2009; Kanekar et al. 2010).

#### 3.1. Line equivalent widths

Because we will rely on them in the analysis, we here seek to verify the robustness and accuracy of the equivalent-width measurements of C I-absorption lines performed in SDSS spectra. For this purpose, we plot in Fig. 2 the measured rest-frame equivalent widths of the C I  $\lambda 1560, 1656$  lines versus each other. It appears that except in one case the strengths of the two lines are in the expected range. This gives confidence in the derived values and their associated uncertainties. In the case of the outlier seen in the lower part of the plot (i.e., at  $z_{\text{abs}} = 1.526$  towards SDSS J 125552.60+223424.4), an unrelated blend to the  $\lambda 1656$  line is a probable reason for the observed deviation.

All the systems are located within about  $2\sigma$  of the boundaries defined by the optically-thin regime on one hand and the relation expected for heavily saturated profiles on the other hand. We note that because of their large equivalent widths ( $W_r \gtrsim 0.4 \text{ \AA}$ ) most of the absorbers, especially those with equivalent-width ratios consistent with the optically-thin regime, are probably made of numerous velocity components.

Here, we assumed that the C I ground-state is solely responsible for the absorption lines while in reality the absorption from the two fine-structure energy levels of the neutral-carbon ground state ( $^3\text{P}_1$  and  $^3\text{P}_2$ ) could in principle contribute mildly to the measured equivalent widths. However, this will affect the equivalent widths of both of the  $\lambda 1560$  and  $\lambda 1656$  lines in the same way so that any departure from the assumed relations due to this blending will be small.

#### 3.2. Completeness

Before discussing the number of C I absorbers per unit redshift ( $n_{\text{C I}}$ ; see the following section), we first need to estimate the completeness of the sample. Given the resolving power  $R$  of the SDSS spectra, the C I  $\lambda 1560$  line rest-frame equivalent width limit is given by:

$$W_{r,\text{lim}}(\lambda 1560) \simeq n \times \frac{1560}{R} \times \text{S/N}^{-1} \quad (1)$$

where  $n = 2$  is the number of standard deviations above which the peak absorption must be detected and  $\text{S/N} > 4$  is the limit on the signal-to-noise ratio per pixel at the corresponding line position. Note that the FWHM of the lines is sampled by two velocity pixels of constant value. Our survey should therefore be complete down to  $W_{r,\text{lim}}(\lambda 1560) \simeq 0.4 \text{ \AA}$ .

We checked the exact level of completeness of our survey at this equivalent-width limit by implementing the following procedure. For this purpose, we used the same data set that we used for the calculation of  $n_{\text{C I}}$  in Sect. 3.3, i.e., the same quasar sample, the same  $[z_{\min}, z_{\max}]$  values and the same mean  $\text{S/N} > 4$  limit. We then randomly selected 1000 QSO spectra and introduced an artificial C I system of rest-frame equivalent width  $W_r(\lambda 1560)$  at different positions in the spectra where the local S/N ratio at both C I lines is larger than four. The distribution of the equivalent width ratio of the  $\lambda 1560$  and  $\lambda 1656$  lines is assumed to be a normal distribution with a dispersion corresponding to what is seen in Fig. 2. Note however that neither the equivalent width ratio nor the exact number of artificial systems used in the simulation has any significant impact on the completeness we infer.

We implemented about 40 000 C I systems that we sought to recover by using the same automatic procedure described in Sect. 2. We varied  $W_r$  over the range 0.1–1.0 Å and defined the completeness as the ratio of the number of recovered systems to

the total number of systems introduced in the spectra. The results are displayed in Fig. 3. It can be seen that the completeness is larger than 80% for  $W_r(\lambda 1560) \geq 0.4 \text{ \AA}$ .

### 3.3. Number of absorbers per unit redshift

We calculated the sensitivity function,  $g(z)$ , of our survey, i.e., the number of lines-of-sight probing a given redshift  $z$  and having  $S/N > 4$  at the expected positions of both C I lines. This function is shown in Fig. 4. It combines together the  $[z_{\min}, z_{\max}]$  pairs, previously defined in Sect. 2, for all the lines-of-sight. We further excluded the regions with velocities relative to the QSO emission redshifts smaller than  $5000 \text{ km s}^{-1}$ , which could, in principle, be influenced by the quasar (see Sect. 3.4). Note that the uncertainties on  $z_{\text{em}}$  are of the order of  $500 \text{ km s}^{-1}$  (see, e.g., Pâris et al. 2012) and therefore are small enough not to affect the statistics. The total statistical absorption path length probed by the QSO sample over  $z = 1.50 - 3.35$  is  $\Delta z \approx 13\,000$  with an average redshift  $\langle z \rangle = 1.9$ . From Fig. 4, it is apparent that the sensitivity of the survey is an increasing function towards lower redshifts. One therefore expects a larger number of absorbers to be found at  $z < 2$ . This is what is observed in practice as indicated by the redshift histogram of the detected intervening C I absorbers over-plotted on the same figure. On the other hand, the small number of C I systems found at  $z_{\text{abs}} > 2.2$  (i.e., eight systems out of a total of 66 systems or, equivalently, 12% of the sample) is striking.

To investigate this further, we calculated the number of intervening C I absorbers per unit redshift,  $n_{\text{C I}}$ , in two redshift bins of roughly equal total absorption path length (with boundary redshift  $z = 1.9$ ). Here, we only considered the systems with rest-frame equivalent widths above the completeness limit of the survey, i.e.,  $W_r(\lambda 1560) \geq 0.4 \text{ \AA}$ . The results are summarised in Table 2 and shown in Fig. 5. In the table, we also separated the strongest from the weaker absorbers (around a median rest-frame equivalent width of  $0.64 \text{ \AA}$ ) but there is no obvious difference between the redshift evolution of these two groups.

The  $n_{\text{C I}} \sim 1.4 \times 10^{-3}$  we measure in the higher redshift bin ( $1.9 < z_{\text{abs}} < 3.35$ ), taking into account the effect of incompleteness estimated in Sect. 3.2, implies that C I systems with  $W_r(\lambda 1560) \geq 0.4 \text{ \AA}$  are more than one hundred-times rarer than DLAs at  $z_{\text{abs}} = 2.5$  (see Noterdaeme et al. 2012). An evolution of  $n_{\text{C I}}$ , with nearly thrice as many systems below  $z = 1.9$  than above that, is also observed. Compared to the redshift behaviour of a non-evolving population, this is significant at the  $4.3\sigma$  level. Such an evolution is interesting and should be studied further as it depends on the balance between dust shielding and the UV radiation field. This may imply a strong evolution of the shielding of 10 eV photons by dust between  $z = 2.5$  and  $z = 1.5$ .

### 3.4. Proximate systems

There are 14 C I systems with velocities relative to the QSO emission redshifts smaller than  $5000 \text{ km s}^{-1}$ . These could be associated with the QSO host galaxy or nearby environment. Six systems even have absorption redshifts larger than the corresponding QSO emission redshifts (by up to  $\sim 4000 \text{ km s}^{-1}$ ) which is difficult to explain by large peculiar velocities in intervening systems. Imposing the same data-quality cuts and minimum equivalent widths as in the previous section, we find that the incidence of C I absorbers at small velocity differences from the quasars is consistent with that of intervening systems.

However, associated errors are large due to small number statistics.

Because of the clustering of galaxies around the massive QSO host galaxies, an excess of proximate C I systems could be expected. However, C I is a fragile species which can easily be photo-ionised by the intense UV radiation emitted by the QSO engine. Interestingly, the lack of a significant excess of proximate systems was also observed by Prochaska et al. (2008) considering DLAs. In this case, the abundance of proximate DLAs is only a factor of two larger than that of the overall DLA population. A similarly low over-abundance factor was observed by Finley et al. (2013) for strong DLAs with  $\log N(\text{H I}) > 21.3$  (atoms  $\text{cm}^{-2}$ ). This is much less than what is expected based on clustering arguments alone.

In this work, we do not observe that the properties of proximate C I systems are different from those of intervening C I systems. This is true for redshift, C I equivalent-width, H I content, reddening and UV bump-strength distributions. Nevertheless, because of the possibly different origin of these absorbers and the possible requirement of strong dust shielding from the nearby QSOs, we discriminate in the following proximate C I systems from the rest of the population and comment, whenever possible, on proximate C I systems of interest.

## 4. Evidence for dust

### 4.1. QSO optical colours

In order to assess the impact of the C I absorbers on their background QSOs and check for the existence of dust in these systems, we first consider the observed colours of these QSOs and compare them with the colours of the overall QSO population used as a control sample.

In Fig. 6, we show the distributions of  $(g - r)$ ,  $(r - i)$  and  $(r - z)$  colours for the 41 696 QSOs whose spectra were searched for C I absorption. In the upper panels of this figure, it is apparent that the lines-of-sight with detected C I absorption do not distribute in the same way as the other lines-of-sight. They are displaced altogether towards redder optical colours compared to the average loci of the QSO redshift sequences. The effect is most easily seen in the lower panels of Fig. 6, which compare the colour histograms of the two QSO populations (i.e., the C I-detected QSO sample and the overall QSO sample). The two-sided Kolmogorov-Smirnov test probability that the two samples are drawn from the same parent distribution is as small as  $\lesssim 10^{-10}$ . The typical colour excess is  $\sim 0.15 \text{ mag}$ , i.e., about five times larger than the mean  $(r - z)$  colour excess of  $0.03 \text{ mag}$  derived by Vladilo et al. (2008) in  $z_{\text{abs}} \approx 2.8$  DLAs from SDSS DR 5. A similar result for DLAs was found by Khare et al. (2012) based on  $(g - i)$  colours of SDSS-DR 7 QSOs. This is clear evidence for the presence of dust among C I absorbers.

### 4.2. Reddening

Motivated by the unequivocal signature of dust in the form of a colour excess of the background QSOs with detected C I absorption, we now aim at constraining the properties and the nature of dust in these systems.

For each of the 66 QSOs with foreground C I absorbers, we derived the QSO reddening,  $E(B-V)$ , following the same approach as used in, e.g., Srianand et al. (2008a) and Noterdaeme et al. (2009a, 2010a). First, we corrected the QSO spectra for Galactic reddening using the extinction maps from Schlegel et al. (1998). We then fitted the spectra with the

SDSS QSO composite spectrum from Vanden Berk et al. (2001) shifted to that QSO emission redshift and reddened with either a Small Magellanic Cloud (SMC), Large Magellanic Cloud (LMC), LMC2 super-shell or Milky Way (MW) extinction law (Gordon et al. 2003) at the C I-absorber redshift. Our procedure is illustrated in the left panel of Fig. 7. The fit with the smallest  $\chi^2$  value indicates the most representative extinction law for a given absorber. The latter is specified in Col. 'Best fit' of Table 3 and the corresponding  $E(B-V)$  value is given in the preceding column.

For each QSO line-of-sight exhibiting C I absorption, we defined a control sample (hereafter denoted as "C.S.") made of SDSS-DR 7 QSOs from the searched sample having an emission redshift within  $\pm 0.05$  and a  $z$ -band magnitude within  $\pm 0.1$  mag from those of the QSO under consideration. In some instances, this resulted in a sample of less than 30 QSOs in which case we increased the above maximum magnitude difference by steps of 0.01 until the number of QSOs in the control sample reached (or exceeded) 30. We then applied to each QSO spectra from the control sample the exact same fitting procedure as described in the previous paragraph. Table 3 lists the number of QSOs and the median reddening and standard deviation of the distribution of  $E(B-V)$  values in each control sample (see the upper right panel of Fig. 7 for an illustration). The values given in Table 3 correspond to the most representative extinction law previously determined for that particular C I-detected QSO spectrum.

In the left panel of Fig. 8, we show the histogram of reddening for the sample of 66 QSO lines-of-sight with detected C I absorbers compared to the cumulative control sample (calculated as the sum of the normalized distributions of individual control samples). As in Sect. 4.1, an offset between the two samples is apparent. The mean reddening induced by C I systems is 0.065 mag. A tail in the histogram of the C I-detected lines-of-sight is observed, with  $E(B-V)$  values up to  $\sim 0.3$  mag.

#### 4.3. The 2175 Å extinction feature

A number of C I-detected QSO spectra are best-matched by an extinction law exhibiting the absorption feature at rest-frame wavelength 2175 Å. In order to measure the strength of this UV bump (denoted  $A_{\text{bump}}$ ), we followed a prescription similar to the one used by Jiang et al. (2010) where the observed QSO spectrum was fitted with the SDSS QSO composite spectrum reddened via a parametrized pseudo-extinction law made of a smooth component and a Drude component. However, here we fixed the wavelength and width of the bump to the Galactic values determined by Fitzpatrick & Massa (2007). Both of these quantities indeed show little variation from line-of-sight to line-of-sight through the Galaxy and the Magellanic Clouds. This then limits the number of free parameters and prevents the fit from diverging towards very wide and shallow solutions which could be non-physical. Indeed, imperfect matching of the observed QSO continuum by the smooth component is expected due to intrinsic QSO-shape variations (e.g., Pitman et al. 2000).

The fitting process is illustrated in the left panel of Fig. 7. The shaded area represents the measure of the bump strength. This is the difference between the above best-fit function and the same function but considering only its smooth component (i.e., with the Drude component set to zero).  $A_{\text{bump}}$  values are listed for each absorber in Table 3. As previously done for the determination of reddening (see Sect. 4.2), we also defined a QSO control sample whose measured  $A_{\text{bump}}$  distribution is shown in the lower right panel of Fig. 7 (i.e., for the given QSO emission

redshift). Table 3 gives for each control sample the median and standard deviation of this distribution.

The histogram of bump strengths in the C I-absorber sample is displayed in the right panel of Fig. 8. One can see from this figure that more than a quarter of the C I systems feature absorption at 2175 Å. This strengthens the result from the previous section that significant reddening of the background QSOs by dust is induced by some of the C I absorbers. We will come back to this and quantify the effect in Sect. 6.

In the following, we shall use the median  $E(B-V)$  and  $A_{\text{bump}}$  values of the control samples, i.e.,  $\langle E(B-V) \rangle_{\text{C.S.}}$  and  $\langle A_{\text{bump}} \rangle_{\text{C.S.}}$ , to define the exact colour excess and bump strength towards a given C I-detected QSO line-of-sight:  $E(B-V) = E(B-V)_{\text{measured}} - \langle E(B-V) \rangle_{\text{C.S.}}$ , and likewise for  $A_{\text{bump}}$ . These zero-point corrections are usually almost negligible (see Table 3). In addition, the standard deviations of  $E(B-V)$  and  $A_{\text{bump}}$  values in each control sample provide an estimate of the uncertainty due to intrinsic QSO-shape variations (see Pitman et al. 2000) and hence the significance of the reddening induced by each C I absorber and the significance of associated 2175 Å absorption, respectively.

## 5. H I content

As part of a spectroscopic campaign which we will describe in a companion paper, we followed up the C I absorbers from the overall sample which are observable from the southern hemisphere using VLT/UVES. We present in Fig. 9 the H I column-density distribution of this C I-absorber sub-sample (referred to in the following as the H I sub-sample) and compare it with the distribution of  $N(\text{H I})$  from systematic DLA and/or sub-DLA surveys.

We secured H I column-density measurements for most of the systems in the overall sample which have a declination of  $\delta < +28$  deg, i.e., 14 out of 16 systems at redshifts  $z_{\text{abs}} > 1.8$  (the two exceptions being the lines-of-sight towards SDSS J091721.37+015448.1 and J233633.81-105841.5) and four out of eight systems at  $z_{\text{abs}} \approx 1.75$  (see Table 1). While H I column densities derived from UVES spectroscopy are usually more accurate, the last two columns of Table 1 show that they confirm those derived directly from SDSS spectra as testified by the five systems at  $z_{\text{abs}} > 2.2$  where this measurement could be done from both datasets. For this reason, we here complement our UVES measurements with the values we derived using SDSS spectra for the three systems at  $z_{\text{abs}} > 2.2$  for which high-resolution spectroscopic data are not available because the background QSOs are too far North for the VLT to observe them. The H I sub-sample thus comprises a total of 21 systems.

In Fig. 9, we compare the observed H I column-density distribution of C I-selected absorbers with that of H I-selected DLAs (from SDSS DR 7 as well; Noterdaeme et al. 2009b). In this figure, we also show the expected number of sub-DLAs using the fitted distribution function from Prochaska et al. (2014). We find that a large fraction of the C I absorbers have neutral atomic-hydrogen column densities slightly below the conventional DLA limit ( $N(\text{H I}) = 2 \times 10^{20}$  atoms  $\text{cm}^{-2}$ ) and therefore classify as strong sub-DLAs. However, the fraction of C I absorbers among sub-DLAs is much less than among DLAs indicating that efficient shielding is much more difficult to obtain below the DLA limit. Though rare, the existence of C I absorbers with low neutral atomic-hydrogen column densities supports the presence of dust in these systems. The dust-to-gas ratio in these systems has to be high enough so that the absorption of UV photons by dust allows C I to be present in large amounts.

No C I system is found with  $\log N(\text{H I}) < 19$  (atoms  $\text{cm}^{-2}$ ). This is a regime where shielding of UV photons becomes extremely difficult even in the presence of dust. However, it is possible that such systems are missed in our search. Indeed, as seen in Fig. 10, there is a trend for neutral atomic-hydrogen column density to increase with C I equivalent width. The gradually decreasing completeness fraction of the survey below  $W_r(\lambda 1560) \approx 0.4 \text{ \AA}$  (see Sect. 2) would therefore preclude low  $N(\text{H I})$  systems from appearing in our sample.

Above the DLA limit, where the incompleteness fraction of our survey is less of an issue, it appears that C I-selected absorbers do not follow the statistics of H I-selected DLAs. Although the number of C I systems with  $\log N(\text{H I}) > 20.3$  (atoms  $\text{cm}^{-2}$ ) is small (i.e., only 9 systems), it is apparent that the overall  $N(\text{H I})$  distribution of C I systems is relatively flat. A two-sided Kolmogorov-Smirnov test applied to all absorbers with  $\log N(\text{H I}) > 20.3$  (atoms  $\text{cm}^{-2}$ ) gives a probability of only 17% that the two distributions come from the same parent population (see inset of Fig. 9). This could be explained by a larger number of velocity components in higher H I column-density gas, thereby increasing the probability of detecting C I. Moreover, large amounts of shielded gas are probably the consequence of the line-of-sight passing through the absorbing galaxy at small impact parameter, in which case we can expect the  $N(\text{H I})$  distribution to be flatter than that of the overall DLA population.

The strongest DLA found among the C I absorbers in the H I sub-sample has  $N(\text{H I}) = 10^{21.8}$  atoms  $\text{cm}^{-2}$ . It is however located at  $z_{\text{abs}} \approx z_{\text{em}}$ . Even ignoring proximate systems, it is yet surprising that three intervening DLAs with  $N(\text{H I}) \geq 10^{21}$  atoms  $\text{cm}^{-2}$  are present in such a small absorber sample. From DLA statistics alone, the probability of randomly selecting three DLAs that strong out of a sample of six DLAs is only 6%. There is therefore a probable excess of strong DLAs among C I absorbers. While the dust content of these systems is significant (see Sects. 4.1 and 4.2), their dust-to-gas ratio must be limited. Indeed, dust reddening and extinction of the background QSOs will inevitably reduce the incidence of strong and dusty DLAs in magnitude-limited QSO samples. This implies that the actual proportion of strong DLAs among C I systems in general is likely to be even higher than what we here found out.

## 6. Empirical relations in the sample

Based on the results presented in the previous sections, we now study the existence of empirical relations between the different quantities measured in this work: neutral atomic-carbon and neutral atomic-hydrogen contents, the reddening C I-selected absorbers induce on their background QSOs and the strength of possible 2175  $\text{\AA}$  extinction features. Because the C I  $\lambda 1560$  transition line is weaker and hence exhibits less saturation than C I  $\lambda 1656$ , we adopt the equivalent width of the former as a proxy for the amount of neutral atomic carbon in the systems.

In Fig. 10, we plot the C I  $\lambda 1560$  rest-frame equivalent width versus  $\log N(\text{H I})$  for the C I absorbers from the H I sub-sample. Both quantities appear to be weakly correlated. A Kendall rank-correlation test indicates the significance of the correlation to be  $1.8\sigma$  only. There is therefore a tendency for strong DLAs to have larger C I equivalent widths but at the same time, for a given H I column density, the C I content can vary substantially from one system to another. Large values of  $W_r(\lambda 1560)$  are observed in DLAs but also in sub-DLAs. The fraction of shielded and probably cold gas could actually be large in some of these sub-DLAs. From the optically-thin approximation applied to the C I  $\lambda 1560$

absorption line and assuming the ionization equilibrium relation,  $N(\text{C I})/N(\text{C II}) \sim 0.01$ , valid for the cold neutral medium (CNM; see, e.g., Jenkins & Tripp 2011), a lower limit on the gas metallicity can be derived:

$$[\text{X}/\text{H}] \gtrsim 18.35 + \log \left( \frac{W_r(\lambda 1560)}{0.01 \times N(\text{H I})} \right) \quad (2)$$

For  $W_r(\lambda 1560) = 0.4 \text{ \AA}$  and  $\log N(\text{H I}) = 20$  (atoms  $\text{cm}^{-2}$ ), the metallicity should be of the order of Solar. More generally, the dashed and dashed-dotted curves in Fig. 10 were calculated using the above equation assuming metallicities of one-tenth of Solar and Solar respectively. Within measurement uncertainties, most of the C I systems lie in between these two curves. If the medium probed by the line-of-sight is a mixture of cold and warm gas, the metallicity of the systems will be even higher. However, if part of the hydrogen is in molecular form, the metallicity will be lower. For the whole C I-absorber sample, Eq. 2 implies a metallicity distribution ranging between  $[\text{X}/\text{H}] = -1.4$  and metallicities in excess of Solar, with a median value of  $[\text{X}/\text{H}] \approx -0.5$ . This means that the metallicities of C I absorbers would on average be at least ten times larger than those of typical DLAs (for the latter, see, e.g., Rafelski et al. (2012)). This should be confirmed by accurate measurements of metal column densities.

In Fig. 11, we display the relation between  $E(\text{B-V})$  and  $\log N(\text{H I})$  among the C I absorbers from the H I sub-sample. Here again, the data points are highly scattered. Most of the systems are associated with low albeit consistently non-zero QSO reddening. Since most of the  $N(\text{H I})$  values are relatively low, the measured amounts of reddening, with median  $E(\text{B-V}) \sim 0.045$ , are actually remarkable. This departs from what is observed in the overall DLA population where the reddening is usually negligible (see, e.g., Vladilo et al. 2008; Khare et al. 2012). The latter authors have shown that DLAs at  $z_{\text{abs}} \approx 2.8$  typically induce a reddening  $E(\text{B-V}) \sim 5 \times 10^{-3}$  mag. Apart from a few outliers, most of the C I systems have reddening properties consistent with those of the Galactic ISM. This is represented in Fig. 11 by the solid line. In the Galaxy, the reddening induced along a line-of-sight is indeed directly proportional to the neutral atomic-hydrogen column density, with  $E(\text{B-V})/N(\text{H}) = 1.63 \times 10^{-22}$  mag atoms $^{-1}$   $\text{cm}^2$  (Gudennavar et al. 2012). Only two C I systems with large  $N(\text{H I})$  are more consistent with what is seen in typical DLAs and/or along SMC lines-of-sight, where the above ratio is smaller than in the Galaxy. Two other C I systems with low  $N(\text{H I})$  might also deviate from the Galactic relation being consistent with a ten-times larger ratio. We caution however that the uncertainties on the reddening measurements are fairly large. If real, this would imply in the latter systems the existence of a grain chemistry more evolved than in the Galaxy with a larger fraction of big grains over very small grains (e.g., Pei 1992). This is opposite to the trend observed in the Magellanic Clouds. In such systems, strong 2175  $\text{\AA}$  absorption is expected. Interestingly, this is what is observed in practice as these two C I systems exhibit two of the strongest three  $A_{\text{bump}}$  values of the H I sub-sample.

To investigate the characteristics of the C I absorbers further, we look in Fig. 12 in more detail at the properties of dust in these systems. In the left panel of this figure,  $E(\text{B-V})$  and  $W_r(\lambda 1560)$  are found to be correlated with each other at the  $4.4\sigma$  significance level. This is noteworthy as different degrees of saturation of the C I  $\lambda 1560$  line are expected to produce scatter in this relation. This implies that the neutral-carbon content of the C I systems is intimately related to the reddening induced along the

line-of-sight or, equivalently, that the amounts of shielded gas and dust are tightly inter-connected. We also note that two of the largest three  $E(B-V)$  values in this plot correspond to systems located at  $z_{\text{abs}} \approx z_{\text{em}}$ . This may however be the result of small number statistics as the reddening induced by the other proximate systems in our sample varies substantially from one system to another.

The relation between  $E(B-V)$  and the UV bump strength,  $A_{\text{bump}}$ , which we previously determined independently from  $E(B-V)$  (see Sect. 4.3), is shown in the right panel of Fig. 12. It can be seen that both quantities are tightly correlated ( $6.0\sigma$ ). A linear least-squares fit (linear correlation coefficient of  $r = 0.77$ ), taking into account errors in both parameters, gives:  $E(B-V) \approx 0.43 \times A_{\text{bump}}$ . The 2175 Å extinction feature is detected at more than  $2\sigma$  (95% confidence level) in about 30% of the C I systems. In such cases, we find  $A_{\text{bump}} \sim 0.4$  and  $E(B-V) \sim 0.2$  mag or, equivalently,  $A_V \sim 0.6$  mag. These values are comparable to what Budzynski & Hewett (2011) have found when targeting the strongest Mg II systems from SDSS DR 6 [ $1 < W_r(\lambda 2796) < 5 \text{ \AA}$ ] where the 2175 Å absorption is detected on a statistical basis only (see also Jiang et al. 2011, for candidate 2175 Å absorption in similar systems). Interestingly, our measured UV bump strengths are also comparable to what has been observed along GRB lines-of-sight at similarly low levels of extinction, e.g., towards GRB 080605 (see Zafar et al. 2012).

In the local Universe, 2175 Å absorption can be observed together with reddening values as low as  $\sim 0.2$  mag (see, e.g., Fitzpatrick & Massa 2007). Even at such low levels of reddening, the UV bump is significantly stronger along Galactic lines-of-sight, i.e., by up to a factor of ten, than in the present C I absorber sample and/or through GRB host galaxies. This discrepancy may be explained if these high-redshift systems probe regions of the ISM affected by a star formation more vigorous than in the Galaxy. A similar argument was proposed by Gordon et al. (2003) with the aim of explaining the variety of LMC and SMC extinction curves. In fact, most of the C I absorbers at the high end of the reddening tail in our sample are best-fit using the extinction law of the LMC2 super-shell near the 30 Dor star-forming region<sup>2</sup> (see left panel of Fig. 8). This means that the far-UV rise of the extinction curve is enhanced and the carriers of the 2175 Å absorption are depleted compared to Galactic lines-of-sight. This is probably the consequence of a high UV flux and/or the mechanical feedback from stars (e.g., Fischera & Dopita 2011) in the vicinity of the C I systems. In contrast, the lack of a UV bump in typical DLAs (e.g., Khare et al. 2012) is probably intrinsic to their low dust and metal contents as the lines-of-sight are likely to pass at large impact parameters from the absorbing galaxy.

The main outlier in the right panel of Fig. 12, which exhibits high reddening but no UV bump, is a proximate system. This is consistent with the above picture where the enhanced UV radiation field from the QSO and/or star-forming regions within the QSO host galaxy are expected to deplete the carriers of the 2175 Å absorption.

## 7. Conclusions

In this work, we presented a new population of QSO absorbers selected directly from the properties of the shielded gas, namely

the strongest C I absorbers, detected in low-resolution QSO spectra from the SDSS-II DR 7 database. These C I absorbers, with  $W_r(\lambda 1560) \geq 0.4 \text{ \AA}$ , are more than one hundred-times rarer than DLAs at  $z_{\text{abs}} = 2.5$ . Their number per unit redshift is increasing significantly below  $z_{\text{abs}} = 2$ , probably coupled to an increase in the star-formation efficiency at these redshifts. Gupta et al. (2012) reported a similarly high detection rate of 21-cm absorbers towards even lower redshifts among strong Mg II systems, which they argued must be related to the evolution of the CNM filling factor in the latter absorbers.

The H I column-density distribution of C I-selected absorbers is flatter than that of H I-selected absorbers. While sub-DLAs have much larger cross-section than DLAs, this can be understood as the shielding of the gas is more difficult at low H I column densities and the number of clouds along the line-of-sight is probably smaller. Cold and dusty gas as traced by C I absorbers is also more likely to be found at small impact parameters from the absorbing galaxies where a flatter  $N(\text{H I})$  distribution is expected. Indeed, despite a likely bias against strong DLAs with large amounts of dust, we find there is among C I systems a probable excess of strong DLAs with  $\log N(\text{H I}) > 21$  (atoms  $\text{cm}^{-2}$ ) compared to systematic DLA searches. This is reminiscent of the  $N(\text{H I})$  distribution of DLAs within GRB host galaxies which is skewed towards extremely strong DLAs (see fig. 10 in Fynbo et al. 2009).

The reddening and therefore the presence of dust along the QSO lines-of-sight with detected C I absorption is directly related to the amount of shielded gas but depends weakly on the total H I column density. The latter can indeed vary by more than a factor of ten for the same C I rest-frame equivalent width. This is probably the consequence of the shielded gas being clumpy while H I absorption samples simultaneously warm diffuse neutral clouds and cold, high-metallicity dusty pockets of gas. The presence of dust inducing significant reddening of the background QSOs and/or 2175 Å extinction features are ubiquitous in about 30% of the C I absorbers. Several systems like these have been found before (see, e.g., Srianand et al. 2008a; Wang et al. 2012). Here, we find that the UV bump is weak compared to Galactic lines-of-sight exhibiting the same amount of reddening. We interpret this as being the consequence of star formation in the vicinity of the systems.

It is likely that the metal and molecular contents of C I absorbers are high and actually higher than those of most DLAs studied till now. High-resolution spectroscopic follow-up observations of the present sample therefore opens up the door to systematic searches for carbon monoxide (CO; see Noterdaeme et al. 2011) and molecules like CN and CH as well as diffuse interstellar bands at high redshift. Such a spectroscopic campaign will be presented in a companion paper. The typical reddening induced by C I absorbers along with the relation between reddening and shielded-gas column density imply that the extinction could be high in some DLAs with C I absorption. If strong dusty DLAs exist, they probably have been missed in the current magnitude-limited QSO samples (see also Boissé et al. 1998; Vladilo et al. 2008). Some of the QSO lines-of-sight identified here, as well as those which may be found by extending the present survey to even larger databases<sup>3</sup>, will result in exceedingly long integration times on high-resolution spectrographs installed on 8-10 m class telescopes. These will however be tar-

<sup>2</sup> Super-giant shells with sizes approaching 1 kpc form the largest structures seen in the ISM of galaxies where large amounts of kinetic energy are contributed by multiple supernovae explosions and energetic stellar winds.

<sup>3</sup> Note that from the Baryon Oscillation Spectroscopic Survey, which is part of SDSS-III, relatively few additional C I systems are expected since the bulk of the new QSOs is at  $z_{\text{em}} \sim 3$ , which provides shorter C I-absorption path length.

gets of choice for the coming generation of Extremely Large Telescopes.

*Acknowledgements.* PN acknowledges support from the ESO Chile visiting scientist programme. RS and PPJ gratefully acknowledge support from the Indo-French Centre for the Promotion of Advanced Research (Centre Franco-Indien pour la Promotion de la Recherche Avancée) under contract No. 4304-2. The authors of this paper also acknowledge the tremendous effort put forth by the Sloan Digital Sky Survey team to produce and release the SDSS survey. Funding for SDSS and SDSS-II has been provided by the Alfred P. Sloan Foundation, the Participating Institutions, the National Science Foundation, the U.S. Department of Energy, the National Aeronautics and Space Administration, the Japanese Monbukagakusho, the Max Planck Society, and the Higher Education Funding Council for England. The SDSS Web Site is <http://www.sdss.org/>. The SDSS is managed by the Astrophysical Research Consortium for the Participating Institutions. The Participating Institutions are the American Museum of Natural History, Astrophysical Institute Potsdam, University of Basel, University of Cambridge, Case Western Reserve University, University of Chicago, Drexel University, Fermilab, the Institute for Advanced Study, the Japan Participation Group, Johns Hopkins University, the Joint Institute for Nuclear Astrophysics, the Kavli Institute for Particle Astrophysics and Cosmology, the Korean Scientist Group, the Chinese Academy of Sciences (LAMOST), Los Alamos National Laboratory, the Max-Planck-Institute for Astronomy (MPIA), the Max-Planck-Institute for Astrophysics (MPA), New Mexico State University, Ohio State University, University of Pittsburgh, University of Portsmouth, Princeton University, the United States Naval Observatory, the University of Washington.

## References

- Abazajian, K. N., Adelman-McCarthy, J. K., Agüeros, M. A., et al. 2009, *ApJS*, 182, 543
- Balashev, S. A., Klimenko, V. V., Ivanchik, A. V., et al. 2014, *ArXiv e-prints*
- Balashev, S. A., Petitjean, P., Ivanchik, A. V., et al. 2011, *MNRAS*, 418, 357
- Boissé, P., Le Brun, V., Bergeron, J., & Deharveng, J.-M. 1998, *A&A*, 333, 841
- Booth, R. S., de Blok, W. J. G., Jonas, J. L., & Fanaroff, B. 2009, *ArXiv e-prints*
- Budzynski, J. M. & Hewett, P. C. 2011, *MNRAS*, 416, 1871
- Duffy, A. R., Meyer, M. J., Staveley-Smith, L., et al. 2012, *MNRAS*, 426, 3385
- Finley, H., Petitjean, P., Pâris, I., et al. 2013, *A&A*, 558, A111
- Fischera, J. & Dopita, M. 2011, *A&A*, 533, A117
- Fitzpatrick, E. L. & Massa, D. 2007, *ApJ*, 663, 320
- Fynbo, J. P. U., Jakobsson, P., Prochaska, J. X., et al. 2009, *ApJS*, 185, 526
- Ge, J. & Bechtold, J. 1999, in *Astronomical Society of the Pacific Conference Series*, Vol. 156, *Highly Redshifted Radio Lines*, ed. C. L. Carilli, S. J. E. Radford, K. M. Menten, & G. I. Langston, 121
- Gordon, K. D., Clayton, G. C., Misselt, K. A., Landolt, A. U., & Wolff, M. J. 2003, *ApJ*, 594, 279
- Gudennavar, S. B., Bubbly, S. G., Preethi, K., & Murthy, J. 2012, *ApJS*, 199, 8
- Gupta, N., Srianand, R., Petitjean, P., et al. 2012, *A&A*, 544, A21
- Gupta, N., Srianand, R., Petitjean, P., Noterdaeme, P., & Saikia, D. J. 2009, *MNRAS*, 398, 201
- Jenkins, E. B. & Tripp, T. M. 2011, *ApJ*, 734, 65
- Jiang, P., Ge, J., Prochaska, J. X., et al. 2010, *ApJ*, 720, 328
- Jiang, P., Ge, J., Zhou, H., Wang, J., & Wang, T. 2011, *ApJ*, 732, 110
- Kanekar, N., Prochaska, J. X., Ellison, S. L., & Chengalur, J. N. 2010, *ApJ*, 712, L148
- Khare, P., vanden Berk, D., York, D. G., Lundgren, B., & Kulkarni, V. P. 2012, *MNRAS*, 419, 1028
- Klimenko, V. V., Balashev, S. A., Ivanchik, A. V., et al. 2015, *MNRAS*, 448, 280
- Krühler, T., Ledoux, C., Fynbo, J. P. U., et al. 2013, *A&A*, 557, A18
- Ledoux, C., Petitjean, P., Fynbo, J. P. U., Møller, P., & Srianand, R. 2006, *A&A*, 457, 71
- Ledoux, C., Petitjean, P., & Srianand, R. 2003, *MNRAS*, 346, 209
- Ledoux, C., Vreeswijk, P. M., Smette, A., et al. 2009, *A&A*, 506, 661
- Madau, P. & Dickinson, M. 2014, *ARA&A*, 52, 415
- Milutinovic, N., Ellison, S. L., Prochaska, J. X., & Tumlinson, J. 2010, *MNRAS*, 408, 2071
- Muller, S., Combes, F., Guélin, M., et al. 2014, *A&A*, 566, A112
- Noterdaeme, P., Ledoux, C., Petitjean, P., & Srianand, R. 2008a, *A&A*, 481, 327
- Noterdaeme, P., Ledoux, C., Srianand, R., Petitjean, P., & López, S. 2009a, *A&A*, 503, 765
- Noterdaeme, P., Petitjean, P., Carithers, W. C., et al. 2012, *A&A*, 547, L1
- Noterdaeme, P., Petitjean, P., Ledoux, C., et al. 2010a, *A&A*, 523, A80
- Noterdaeme, P., Petitjean, P., Ledoux, C., & Srianand, R. 2009b, *A&A*, 505, 1087
- Noterdaeme, P., Petitjean, P., Ledoux, C., Srianand, R., & Ivanchik, A. 2008b, *A&A*, 491, 397
- Noterdaeme, P., Petitjean, P., Srianand, R., Ledoux, C., & López, S. 2011, *A&A*, 526, L7
- Noterdaeme, P., Srianand, R., & Mohan, V. 2010b, *MNRAS*, 403, 906
- Pâris, I., Petitjean, P., Aubourg, É., et al. 2012, *A&A*, 548, A66
- Pei, Y. C. 1992, *ApJ*, 395, 130
- Petitjean, P., Ledoux, C., Noterdaeme, P., & Srianand, R. 2006, *A&A*, 456, L9
- Petitjean, P., Srianand, R., & Ledoux, C. 2000, *A&A*, 364, L26
- Petitjean, P., Srianand, R., & Ledoux, C. 2002, *MNRAS*, 332, 383
- Pettini, M. 2006, in *The Fabulous Destiny of Galaxies: Bridging Past and Present*, ed. V. Le Brun, A. Mazure, S. Arnouts, & D. Burgarella, 319
- Pitman, K. M., Clayton, G. C., & Gordon, K. D. 2000, *PASP*, 112, 537
- Prochaska, J. X., Hennawi, J. F., & Herbert-Fort, S. 2008, *ApJ*, 675, 1002
- Prochaska, J. X., Herbert-Fort, S., & Wolfe, A. M. 2005, *ApJ*, 635, 123
- Prochaska, J. X., Madau, P., O'Meara, J. M., & Fumagalli, M. 2014, *MNRAS*, 438, 476
- Quider, A. M., Nestor, D. B., Turnshek, D. A., et al. 2011, *AJ*, 141, 137
- Rafelski, M., Wolfe, A. M., Prochaska, J. X., Neeleman, M., & Mendez, A. J. 2012, *ApJ*, 755, 89
- Schlegel, D. J., Finkbeiner, D. P., & Davis, M. 1998, *ApJ*, 500, 525
- Schneider, D. P., Richards, G. T., Hall, P. B., et al. 2010, *AJ*, 139, 2360
- Snow, T. P. & McCall, B. J. 2006, *ARA&A*, 44, 367
- Srianand, R., Gupta, N., Petitjean, P., et al. 2012, *MNRAS*, 421, 651
- Srianand, R., Gupta, N., Petitjean, P., Noterdaeme, P., & Saikia, D. J. 2008a, *MNRAS*, 391, L69
- Srianand, R., Noterdaeme, P., Ledoux, C., & Petitjean, P. 2008b, *A&A*, 482, L39
- Srianand, R., Petitjean, P., Ledoux, C., Ferland, G., & Shaw, G. 2005, *MNRAS*, 362, 549
- Vanden Berk, D. E., Richards, G. T., Bauer, A., et al. 2001, *AJ*, 122, 549
- Vladilo, G., Prochaska, J. X., & Wolfe, A. M. 2008, *A&A*, 478, 701
- Wang, J.-G., Zhou, H.-Y., Ge, J., et al. 2012, *ApJ*, 760, 42
- Wolfe, A. M., Gawiser, E., & Prochaska, J. X. 2005, *ARA&A*, 43, 861
- York, D. G., Adelman, J., Anderson, Jr., J. E., et al. 2000, *AJ*, 120, 1579
- Zafar, T., Watson, D., Elíasdóttir, A., et al. 2012, *ApJ*, 753, 82
- Zwaan, M. A. & Prochaska, J. X. 2006, *ApJ*, 643, 675



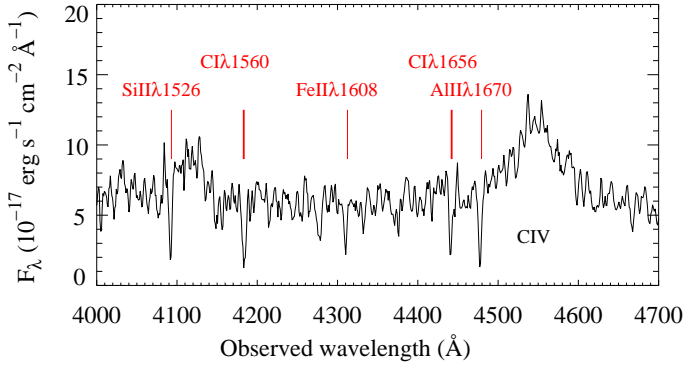


**Fig. 1.** SDSS spectrum of the  $z_{\text{em}} = 1.94$  QSO J0815+2640. The C I  $\lambda\lambda 1560, 1656$  absorption lines detected at  $z = 1.681$  are indicated along with several low-ionization metal lines at the same redshift. Among the latter, the simultaneous presence of Si II  $\lambda 1526$  and Al II  $\lambda 1670$  lines was required by our detection algorithm to minimize the probability of chance coincidences. In this system, Fe II  $\lambda 1608$  absorption is also observed even though relatively weak.

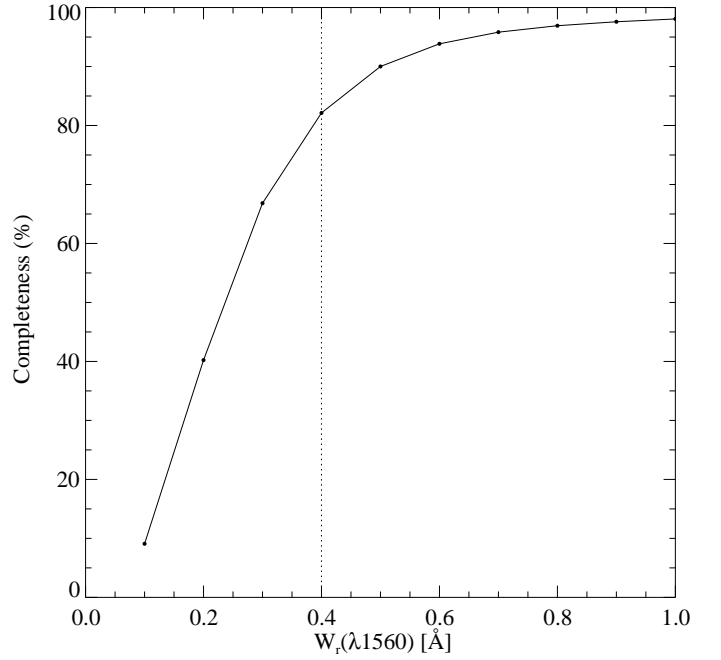


**Fig. 3.** Completeness of our C I search as a function of the C I  $\lambda 1560$  rest-frame equivalent width. Each point is based on a total of 40 000 artificial C I systems introduced in 1000 randomly-selected SDSS QSO spectra. The vertical dotted line shows our chosen completeness limit of  $W_r(\lambda 1560) = 0.4 \text{ \AA}$ .

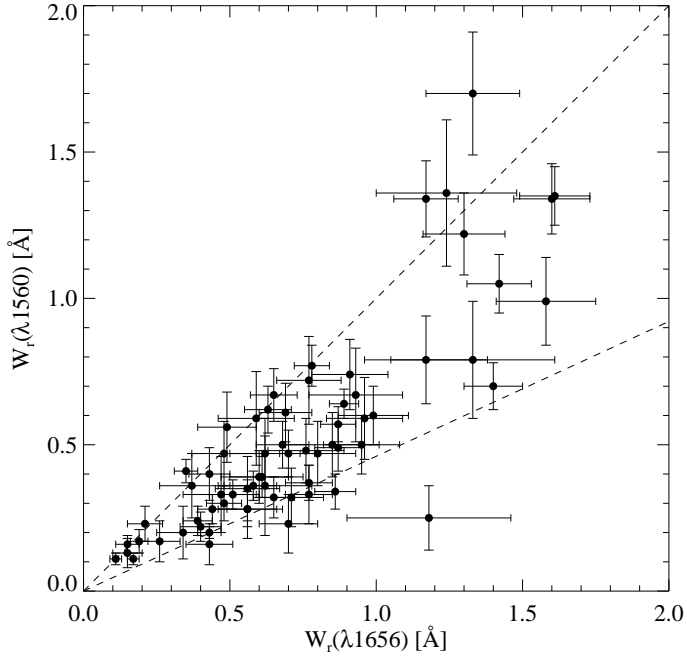


**Fig. 2.** Rest-frame equivalent widths of C I absorption lines measured in SDSS spectra and associated  $1\sigma$  uncertainties. The upper dashed line shows the 1:1 relation expected in case of heavily saturated profiles. The lower dashed line shows the expectation for absorption lines on the linear part of the curve-of-growth.

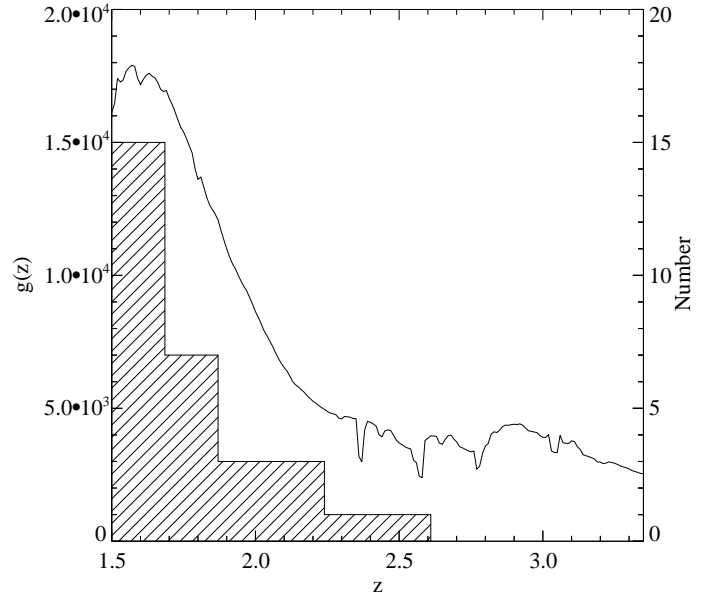


**Fig. 4.** Statistical sensitivity function of our C I survey,  $g(z)$  (solid curve; left-hand side axis). The dips seen at  $z \sim 2.35$  (resp. 2.6) are due to C I  $\lambda 1656$  (resp. C I  $\lambda 1560$ ) falling over bad pixels at the junction between the two SDSS CCD chips. Dips at higher redshifts ( $z \sim 2.8, 3.05$ ) are due to telluric lines (e.g., [O I]  $\lambda 6300$ ). The hashed histogram (right-hand side axis) shows the C I-absorber number counts in different redshift bins for intervening systems with rest-frame equivalent width above the completeness limit of the survey, i.e.,  $W_r(\lambda 1560) \geq 0.4 \text{ \AA}$ .

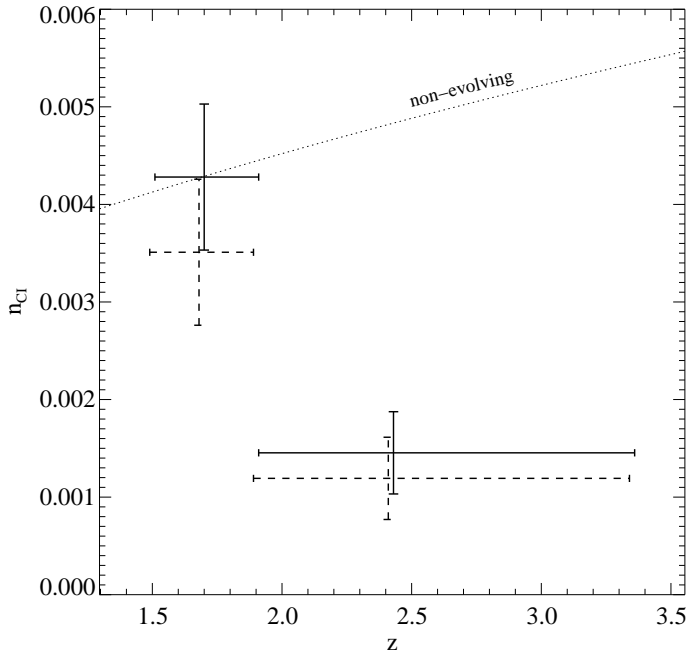


**Fig. 5.** Evolution of the number of intervening C I absorbers per unit redshift,  $n_{\text{C I}}$ , for systems with rest-frame equivalent widths  $W_{\text{r}}(\lambda 1560) \geq 0.4 \text{ \AA}$ . **The measurements (solid) are corrected for incompleteness at the latter limit. For clarity purposes, the uncorrected data (dashed) are displayed with a slight offset in abscissa.** The dotted curve shows the expected redshift behaviour of a non-evolving population.

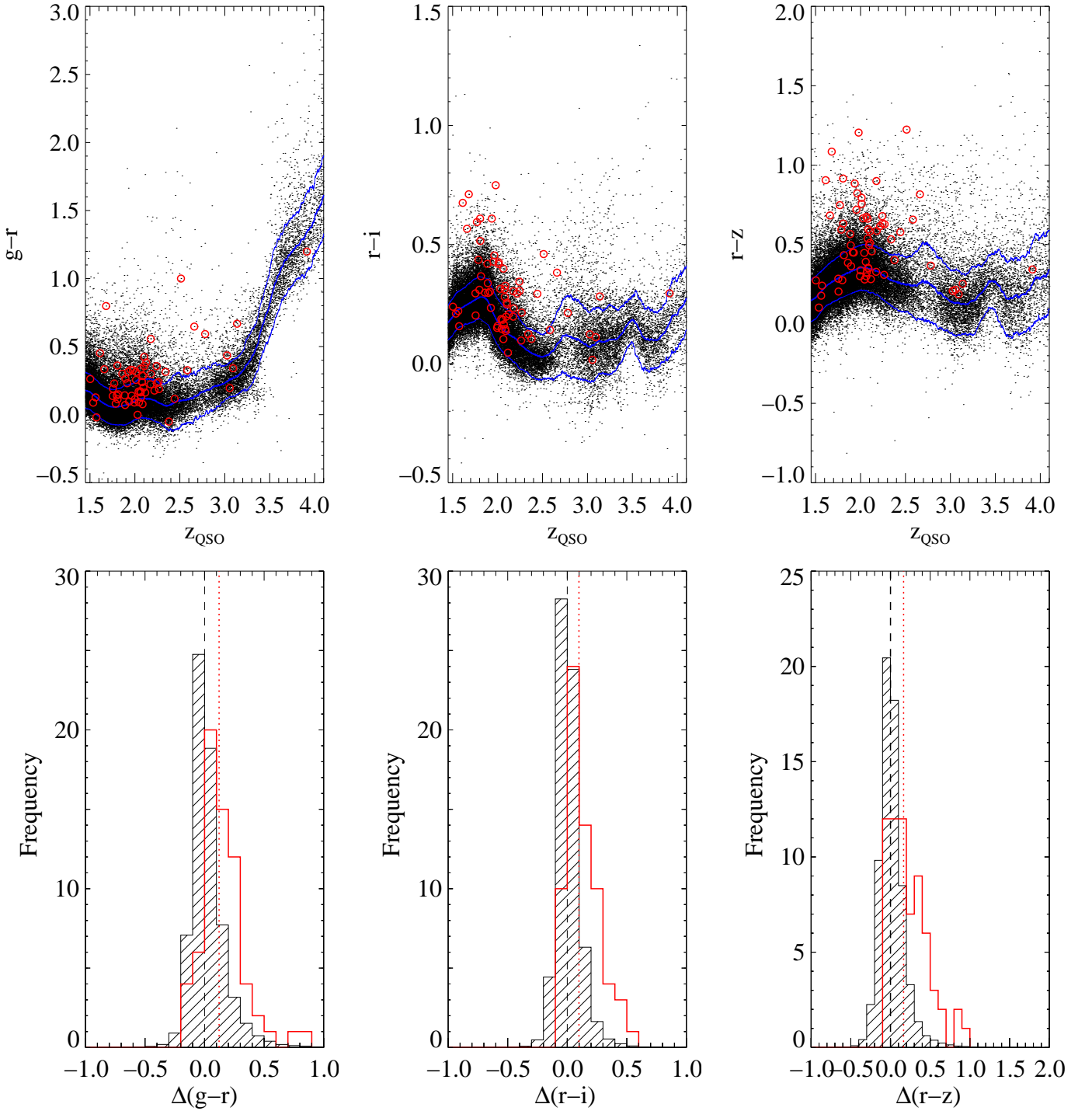


**Fig. 6.** *Upper panels:* Colours of the 41 696 SDSS QSOs whose spectra were searched for C I absorption versus QSO emission redshift.  $(g-r)$ ,  $(r-i)$  and  $(r-z)$  colours are displayed in the left, middle and right-hand side panels, respectively. The thick blue line shows the median QSO colour as a function of redshift. Thin blue lines are shown one standard deviation away from that median. The red circles indicate the 66 lines-of-sight passing through C I-bearing gas. *Lower panels:* Distribution of colour excesses [defined as, e.g.:  $(g-r) - \langle g-r \rangle_{z_{\text{QSO}}}$  for  $\Delta(g-r)$ ] for the 66 QSOs whose spectra were found to exhibit C I absorption (thick red histogram) compared to the whole QSO sample (thin-hashed histogram, scaled down by a factor of 632 to have the same area). In each panel [from left to right:  $\Delta(g-r)$ ,  $\Delta(r-i)$  and  $\Delta(r-z)$ ], vertical dotted red lines indicate the median colour excesses of the sample of QSOs with detected C I absorption. The median values for the whole QSO sample are shown by vertical dashed lines.

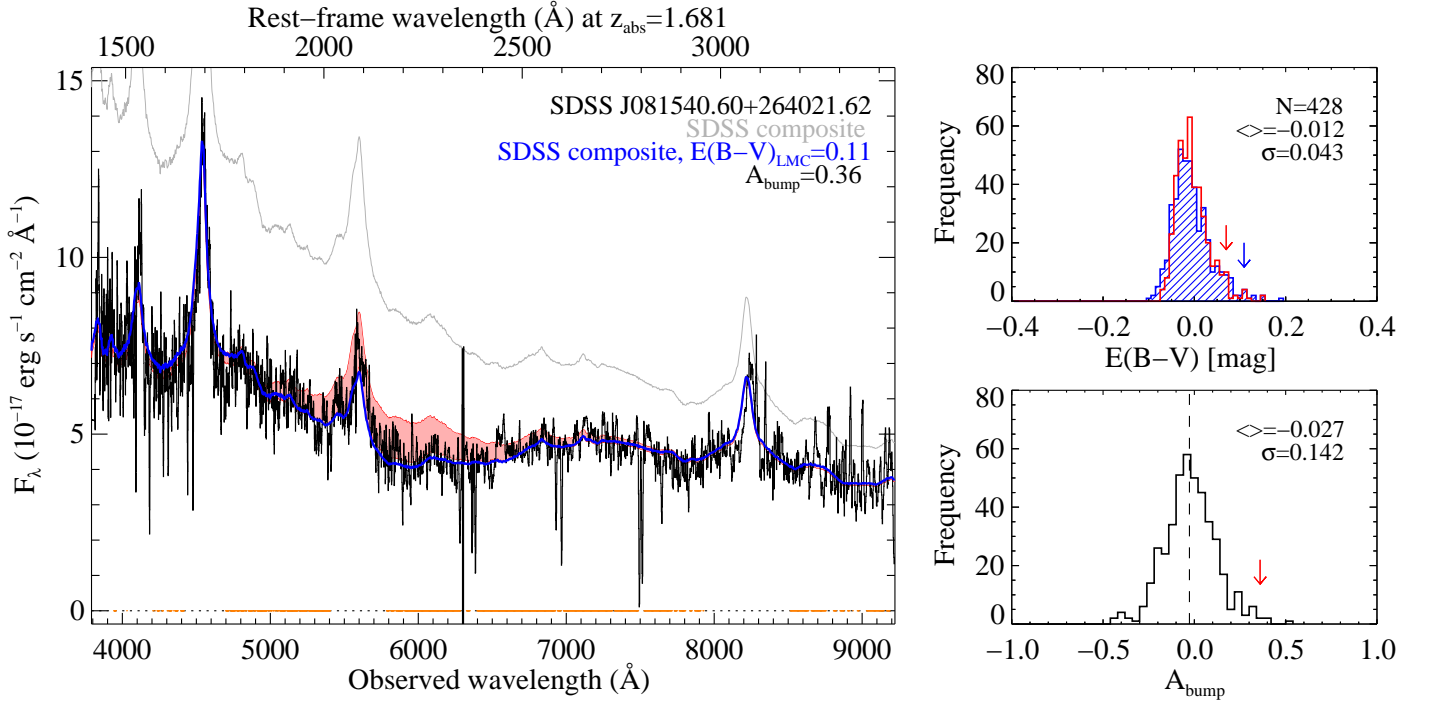


**Fig. 7.** *Left panel:* Illustration of reddening measurement based on QSO SED fitting. The blue curve shows our best fit to QSO continuum using the QSO template spectrum from Vanden Berk et al. (2001) and the best-fitting LMC extinction law at the redshift of the C I absorber. The non-extinguished QSO template is displayed in grey. The additional presence of a 2175 Å absorption feature is shown by the light-red shaded area (i.e.,  $A_{\text{bump}}$ ). The broken orange line at zero ordinate indicates the wavelength regions devoid of QSO emission lines, strong absorption lines and sky residuals, which were used during the  $\chi^2$  minimization. *Upper right panel:* Distribution of reddening measured in the QSO control sample assuming either a SMC (red) or the best-fitting extinction law (in this case, LMC; blue). The reddening values of the sight-line under consideration are indicated by downward arrows. *Lower right panel:* Same as above but for the distribution of 2175 Å bump strengths.

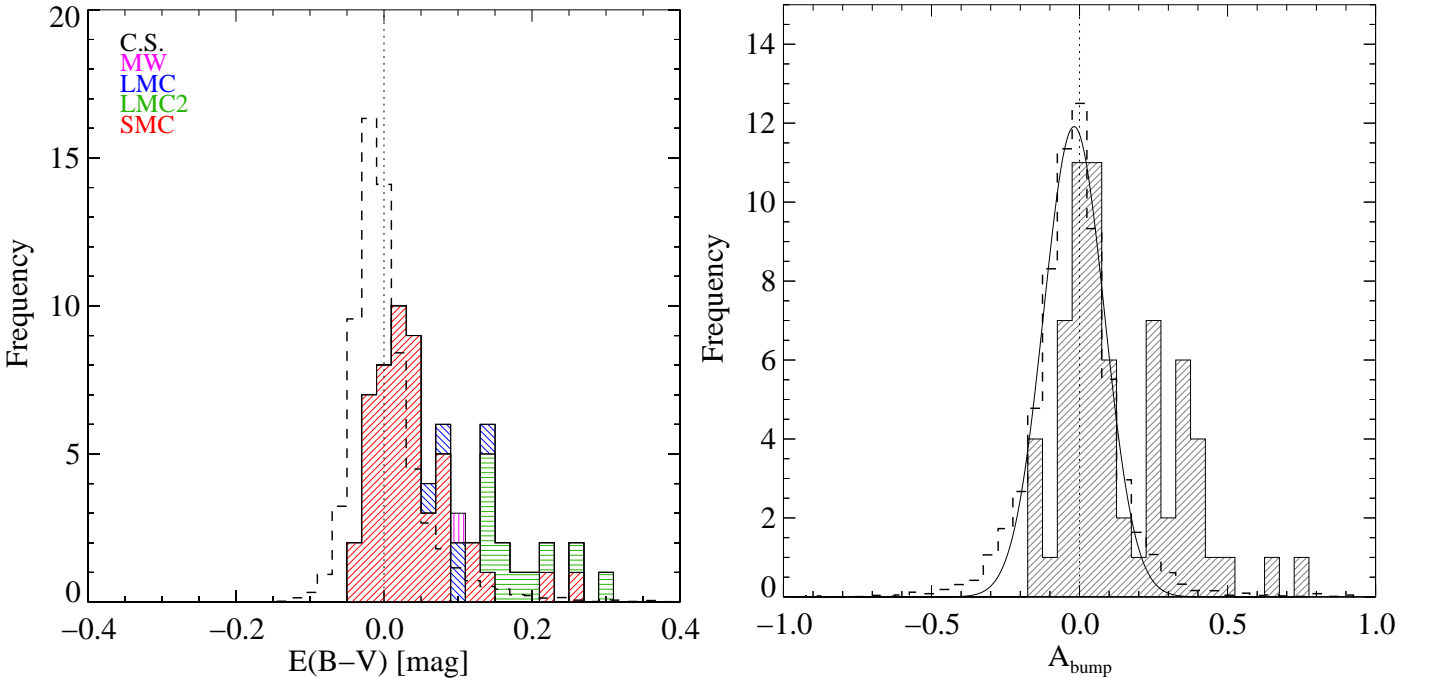


**Fig. 8.** *Left panel:* Histogram of reddening for the sample of 66 QSOs whose spectra were found to exhibit C I absorption (multi-color). The colour/hash coding for the different C I-detected lines-of-sight relates to the best-fitting extinction law (red: SMC; blue: LMC; green: LMC2; purple: MW). The distribution of reddening from the QSO control sample (C.S.), i.e., the sum of the normalized distributions of individual QSO control samples, is displayed with dashed lines. *Right panel:* Same as in the left panel but for the histogram of 2175 Å bump strengths. The distribution from the QSO control sample is well represented by a Gaussian profile (solid curve).

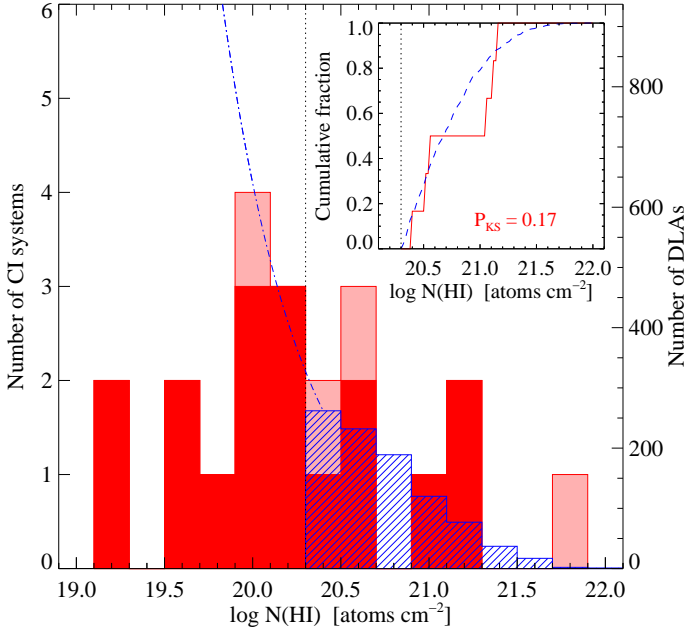


**Fig. 9.** Neutral atomic-hydrogen column-density distribution of C I absorbers (red-filled histogram; left-hand side axis). Proximate systems are displayed in salmon. The  $N(\text{H I})$  distribution of intervening DLAs from SDSS DR7 (Noterdaeme et al. 2009b, blue-hashed histogram) is over-plotted using a different scaling (right-hand side axis) so that the areas of the two histograms above  $\log N(\text{H I}) = 20.3$  are equal. The blue dashed-dotted curve is a fit of the distribution in the sub-DLA regime from Prochaska et al. (2014). The inset shows the cumulative  $N(\text{H I})$  distributions of the intervening C I and DLA samples starting at  $\log N(\text{H I}) = 20.3$  (atoms  $\text{cm}^{-2}$ ) and the two-sided Kolmogorov-Smirnov test probability that the two distributions come from the same parent population.

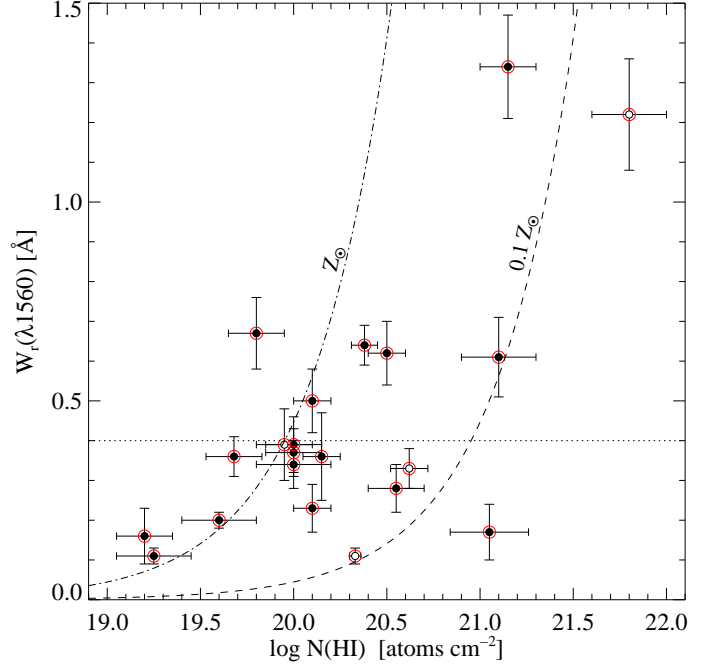


**Fig. 10.** C I  $\lambda 1560$  rest-frame equivalent width versus  $N(\text{H I})$ , the neutral atomic-hydrogen column density of C I absorbers. Intervening (resp. proximate) systems are displayed as filled (resp. empty) black circles. Data points are encircled in red as they correspond to the sub-sample of C I systems with measured  $N(\text{H I})$ , i.e., the H I sub-sample. The dashed (resp. dashed-dotted) curve materializes the limit above which systems are expected to have in excess of one-tenth of Solar (resp. in excess of Solar) metallicity (see text). The completeness limit of the survey is indicated by the horizontal line.

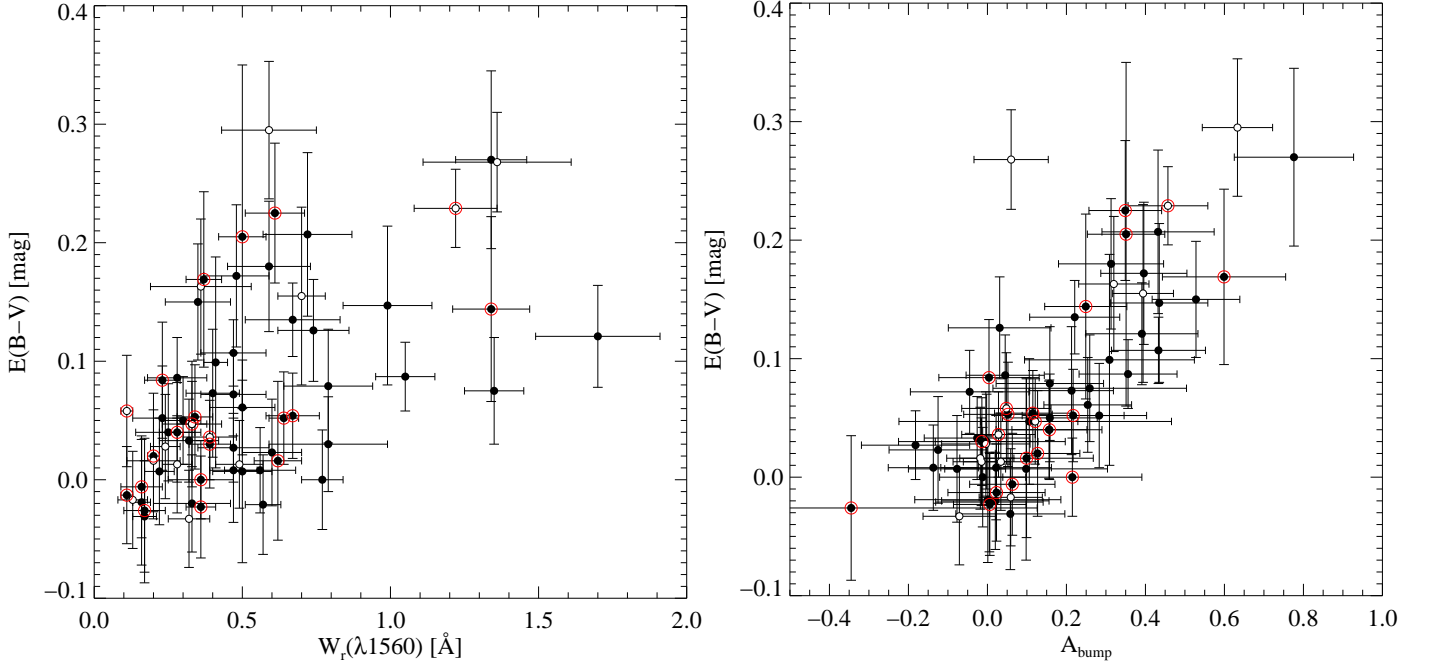


**Fig. 12.** *Left panel:* Reddening of the background QSOs with detected C I absorption (overall sample) versus C I  $\lambda 1560$  rest-frame equivalent width. Symbol conventions are the same as in Fig. 10. Data points encircled in red correspond to the H I sub-sample. *Right panel:* Same as in the left panel with the exception that reddening is plotted against 2175 Å bump strength.

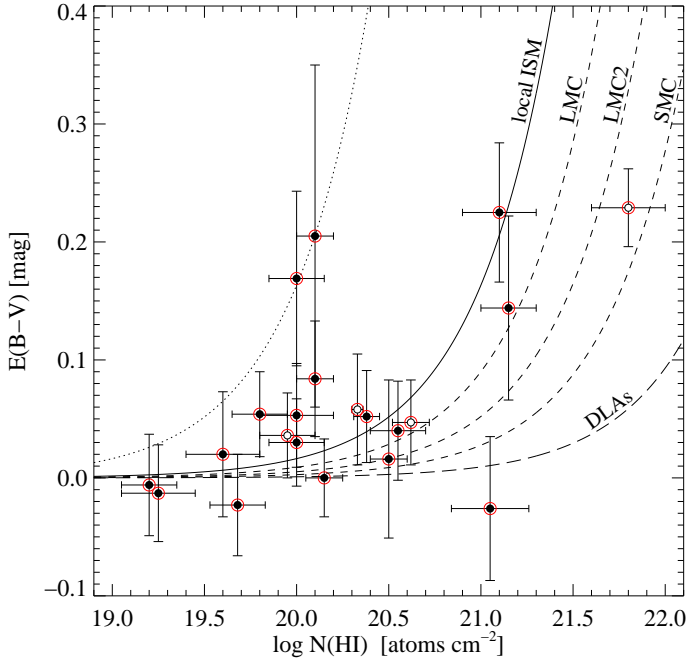


**Fig. 11.** Reddening of the background QSOs with detected C I absorption versus  $N(\text{H I})$  of the C I absorbers. Symbol conventions are the same as in Fig. 10. The solid line shows the relation observed in the local ISM where  $E(\text{B-V})/N(\text{H}) = 1.63 \times 10^{-22}$  mag atoms $^{-1}$  cm $^2$  (Gudennavar et al. 2012). The dotted line illustrates a reddening per hydrogen atom ten times higher than that. The dashed curves correspond to the observations of the Magellanic Clouds (Gordon et al. 2003). The long-dashed line shows the relation derived for typical DLAs at  $z_{\text{abs}} \approx 2.8$  (e.g., Vladilo et al. 2008; Khare et al. 2012).

**Table 1.** C I systems identified in SDSS-DR7 QSO spectra.

QSO name	plate	MJD	fibre	$z_{\text{em}}$	$z_{\text{abs}}$	$W_r(\lambda 1560)^a$ [Å]	$W_r(\lambda 1656)^a$ [Å]	S/N <sup>b</sup>	$\log N(\text{H I})_{\text{SDSS}}^c$ [atoms cm <sup>-2</sup> ]	$\log N(\text{H I})_{\text{UVES}}^d$ [atoms cm <sup>-2</sup> ]
J021606.13–002104.9	0405	51816	114	2.22	1.737	0.33 ± 0.10	0.77 ± 0.08	14	...	...
J030049.24–072137.8	0458	51929	437	2.11	1.536	0.79 ± 0.15	1.17 ± 0.21	5	...	...
J080801.74+330009.2	0825	52289	166	1.90	1.888	0.24 ± 0.05	0.39 ± 0.05	18	...	...
J081116.06+083837.7	2570	54081	566	2.07	1.906	0.23 ± 0.06	0.21 ± 0.06	15	...	20.10 ± 0.10
J081540.60+264021.6	1266	52709	355	1.94	1.681	1.70 ± 0.21	1.33 ± 0.16	5	...	...
J082003.40+155932.9	2272	53713	378	1.95	1.547	0.72 ± 0.15	0.77 ± 0.11	7	...	...
J085206.65+193548.4	2281	53711	452	1.91	1.788	0.34 ± 0.06	0.86 ± 0.07	13	...	20.00 ± 0.20
J085437.60+031734.8	0565	52225	480	2.24	1.567	0.40 ± 0.09	0.43 ± 0.07	12	...	...
J085726.79+185524.3	2281	53711	630	1.89	1.730	0.20 ± 0.02	0.43 ± 0.04	33	...	19.60 ± 0.20
J090558.75+553039.2	0450	51908	470	1.57	1.579	0.13 ± 0.05	0.15 ± 0.05	16	...	...
J090942.56+532126.5	0553	51999	425	2.07	1.628	0.47 ± 0.08	0.70 ± 0.09	12	...	...
J091516.27+071750.9	1194	52703	506	2.38	1.681	0.50 ± 0.10	0.95 ± 0.13	11	...	...
J091721.37+015448.1	0473	51929	426	2.18	2.107	0.67 ± 0.16	0.93 ± 0.16	5	...	...
J092759.79+154321.8	2579	54068	364	1.81	1.731	0.61 ± 0.10	0.69 ± 0.09	9	...	21.10 ± 0.20
J094529.37+552525.7	0556	51991	045	2.24	1.867	0.74 ± 0.12	0.91 ± 0.13	7	...	...
J095114.97+545736.5	0769	52282	458	1.80	1.613	0.77 ± 0.07	0.78 ± 0.06	14	...	...
J101544.34+310617.2	1953	53358	604	1.56	1.596	0.20 ± 0.09	0.34 ± 0.09	9	...	...
J104705.76+205734.5	2478	54097	558	2.01	1.775	0.59 ± 0.14	0.96 ± 0.13	7	...	...
J105436.96+542343.7	0907	52373	129	1.50	1.513	0.49 ± 0.08	0.87 ± 0.08	10	...	...
J105746.42+662250.5	0490	51929	179	2.34	2.088	0.30 ± 0.06	0.48 ± 0.06	13	...	...
J111756.53+143716.9	1753	53383	353	2.09	2.001	0.67 ± 0.09	0.65 ± 0.08	10	...	19.80 ± 0.15
J112250.95+143732.5	1753	53383	477	2.05	1.554	0.17 ± 0.04	0.19 ± 0.03	28	...	...
J112913.29–023740.9	0327	52294	308	1.86	1.623	0.60 ± 0.10	0.99 ± 0.12	8	...	...
J113341.29–005740.1	0282	51658	215	1.68	1.706	1.36 ± 0.25	1.24 ± 0.24	4	...	...
J114141.84+444206.1	1367	53083	499	1.96	1.903	0.48 ± 0.11	0.76 ± 0.13	7	...	...
J115153.87+150945.0	1762	53415	495	3.05	2.400	0.36 ± 0.11	0.37 ± 0.11	7	20.15 ± 0.33 <sup>e</sup>	20.15 ± 0.10
J115705.51+615521.7	0777	52320	107	2.51	2.460	1.22 ± 0.14	1.30 ± 0.14	7	21.80 ± 0.20 <sup>f</sup>	...
J120935.79+671715.7	0493	51957	178	2.03	1.843	0.47 ± 0.11	0.48 ± 0.11	8	...	...
J122825.67+303038.6	2234	53823	430	3.91	3.098	0.17 ± 0.07	0.26 ± 0.07	11	21.05 ± 0.21 <sup>e</sup>	...
J123714.61+064759.6	1628	53474	193	2.78	2.691	0.37 ± 0.06	0.77 ± 0.08	14	20.15 ± 0.28 <sup>e</sup>	20.00 ± 0.15 <sup>g</sup>
J124708.43+500320.8	1278	52735	039	2.27	2.135	1.05 ± 0.10	1.42 ± 0.11	9	...	...
J124829.71+284858.1	2239	53726	219	1.54	1.513	0.32 ± 0.07	0.65 ± 0.07	12	...	...
J124841.45+302433.0	2239	53726	469	2.06	1.691	0.57 ± 0.06	0.87 ± 0.06	15	...	...
J125552.60+223424.4	2649	54212	507	1.82	1.526	0.25 ± 0.11	1.18 ± 0.28	8	...	...
J130225.28+211158.6	2650	54505	296	1.76	1.656	0.56 ± 0.12	0.49 ± 0.10	8	...	...
J130628.87+281550.8	2009	53904	288	2.10	2.012	0.28 ± 0.10	0.56 ± 0.10	8	...	...
J130828.43+584000.6	0958	52410	224	3.09	2.473	0.39 ± 0.07	0.61 ± 0.14	11	20.00 ± 0.15	...
J131129.11+222552.6	2651	54507	398	3.14	3.093	0.33 ± 0.05	0.51 ± 0.08	16	20.50 ± 0.10	20.62 ± 0.10
J131400.57+054319.5	0850	52338	620	1.89	1.583	0.23 ± 0.10	0.70 ± 0.10	8	...	...
J134122.51+185214.0	2642	54232	494	2.00	1.544	0.16 ± 0.03	0.15 ± 0.04	27	...	...
J134601.10+064408.4	1803	54152	074	2.09	1.512	0.79 ± 0.20	1.33 ± 0.28	6	...	...
J135122.00+461828.5	1466	53083	416	1.81	1.606	0.99 ± 0.15	1.58 ± 0.17	10	...	...
J141550.47+300146.9	2129	54252	288	2.08	1.676	1.35 ± 0.10	1.61 ± 0.12	13	...	...
J141606.79+180403.2	2759	54534	359	2.13	1.622	0.47 ± 0.11	0.80 ± 0.13	8	...	...
J143243.93+330746.7	1841	53491	513	2.09	2.058	0.28 ± 0.05	0.44 ± 0.05	17	...	...
J143657.87+291100.6	2138	53757	259	1.77	1.596	0.35 ± 0.11	0.56 ± 0.11	8	...	...
J143912.05+111740.6	1711	53535	374	2.58	2.418	0.50 ± 0.08	0.68 ± 0.09	10	20.27 ± 0.24 <sup>e</sup>	20.10 ± 0.10 <sup>h</sup>
J144929.27+333811.0	1646	53498	065	2.17	2.021	0.47 ± 0.12	0.62 ± 0.12	7	...	...
J145432.54+343523.9	1384	53121	269	1.61	1.580	0.59 ± 0.16	0.59 ± 0.13	6	...	...
J145953.25+012944.2	0538	52029	039	1.66	1.623	0.36 ± 0.17	0.62 ± 0.16	5	...	...
J150738.73+415530.6	1291	52735	505	1.79	1.674	0.50 ± 0.11	0.85 ± 0.16	7	...	...
J152209.12+083020.0	1721	53857	192	1.93	1.627	0.32 ± 0.10	0.71 ± 0.11	8	...	...
J160320.76+170117.8	2200	53875	318	1.99	1.890	0.16 ± 0.07	0.43 ± 0.08	12	...	19.20 ± 0.15
J160457.51+220300.5	2205	53793	328	1.98	1.641	1.34 ± 0.12	1.60 ± 0.13	7	...	...
J161526.65+264813.8	1576	53496	394	2.18	2.118	0.28 ± 0.06	0.56 ± 0.12	15	...	20.55 ± 0.15
J162321.43+135532.4	2202	53566	132	1.75	1.751	0.39 ± 0.09	0.60 ± 0.10	9	...	19.95 ± 0.15
J164610.20+232923.0	1424	52912	301	2.06	1.998	0.36 ± 0.05	0.58 ± 0.08	15	...	19.68 ± 0.15
J170542.92+354340.4	0974	52427	561	2.01	2.038	0.70 ± 0.08	1.40 ± 0.10	10	...	...
J212329.47–005053.0	0987	52523	103	2.26	2.060	0.11 ± 0.02	0.11 ± 0.02	41	...	19.25 ± 0.20 <sup>i</sup>

<sup>a</sup> Rest-frame equivalent width of the absorption detected at the position of the C I lines (measurements drawn from SDSS spectra).<sup>b</sup> Average signal-to-noise ratio per pixel around the C I lines.<sup>c</sup> Neutral atomic-hydrogen column density of the systems measured from Ly $\alpha$  absorption in SDSS spectra.<sup>d</sup>  $N(\text{H I})$  values derived from follow-up UVES spectroscopy.<sup>e</sup> Noterdaeme et al. (2009b); <sup>f</sup> Wang et al. (2012); <sup>g</sup> Noterdaeme et al. (2010a); <sup>h</sup> Noterdaeme et al. (2008b); <sup>i</sup> Milutinovic et al. (2010); <sup>j</sup> Ledoux et al. (2006).

**Table 1.** *continued.*

QSO name	plate	MJD	fibre	$z_{\text{em}}$	$z_{\text{abs}}$	$W_r(\lambda 1560)^a$ [Å]	$W_r(\lambda 1656)^a$ [Å]	S/N <sup>b</sup>	$\log N(\text{H I})_{\text{SDSS}}^c$ [atoms cm <sup>-2</sup> ]	$\log N(\text{H I})_{\text{UVES}}^d$ [atoms cm <sup>-2</sup> ]
J222910.16+141402.2	0738	52521	382	2.11	1.586	0.33 ± 0.13	0.47 ± 0.13	6	...	...
J225719.04-100104.7	0724	52254	150	2.08	1.836	0.64 ± 0.05	0.89 ± 0.05	17	...	20.38 ± 0.07
J233133.05-090246.6	0646	52523	619	2.44	1.734	0.41 ± 0.04	0.35 ± 0.04	20	...	...
J233156.49-090802.0	0646	52523	616	2.66	2.143	1.34 ± 0.13	1.17 ± 0.11	8	...	21.15 ± 0.15
J233633.81-105841.5	0647	52553	201	2.04	1.829	0.22 ± 0.05	0.40 ± 0.07	15	...	...
J234023.67-005327.1	0385	51877	204	2.09	2.054	0.11 ± 0.02	0.17 ± 0.02	37	...	20.33 ± 0.03
J235057.87-005210.0	0386	51788	137	3.03	2.426	0.62 ± 0.08	0.63 ± 0.08	11	20.39 ± 0.27 <sup>e</sup>	20.50 ± 0.10 <sup>j</sup>

<sup>a</sup> Rest-frame equivalent width of the absorption detected at the position of the C I lines (measurements drawn from SDSS spectra).

<sup>b</sup> Average signal-to-noise ratio per pixel around the C I lines.

<sup>c</sup> Neutral atomic-hydrogen column density of the systems measured from Ly $\alpha$  absorption in SDSS spectra.

<sup>d</sup>  $N(\text{H I})$  value derived from follow-up UVES spectroscopy.

<sup>e</sup> Noterdaeme et al. (2009b); <sup>f</sup> Wang et al. (2012); <sup>g</sup> Noterdaeme et al. (2010a); <sup>h</sup> Noterdaeme et al. (2008b); <sup>i</sup> Milutinovic et al. (2010); <sup>j</sup> Ledoux et al. (2006).

**Table 2.** Intervening C I-absorber number counts.

C I samples	$W_r(\lambda 1560)$ [Å]	$z_{\text{min}}$	$z_{\text{max}}$	$\Delta z$	# of C I	$n_{\text{C I}}^a$ ( $\times 10^{-3}$ )
All systems	$\geq 0.4$	1.5	1.9	6268	22	3.5 ± 0.8
		1.9	3.35	6710	8	1.2 ± 0.4
Strongest	$\geq 0.64$	1.5	1.9	6268	10	1.6 ± 0.5
		1.9	3.35	6710	4	0.6 ± 0.3
Weaker	$\geq 0.4, < 0.64$	1.5	1.9	6268	12	1.9 ± 0.6
		1.9	3.35	6710	4	0.6 ± 0.3

<sup>a</sup> Prior to correcting for incompleteness (i.e., ~ 18% at  $W_r(\lambda 1560) = 0.4$  Å).



**Table 3.** SED fitting of QSO spectra with detected C I absorbers.

QSO name	$z_{\text{em}}$	$z_{\text{abs}}$	$E(B-V)$ [mag]	best fit	$A_{\text{bump}}$	C.S. <sup>a</sup> :	$E(B-V)$ [mag]		$A_{\text{bump}}$	
						$N_{\text{QSO}}$	median	$\sigma$	median	$\sigma$
J021606.13-002104.9	2.22	1.737	0.039	SMC	0.097	173	-0.008	0.053	-0.009	0.123
J030049.24-072137.8	2.11	1.536	0.075	SMC	0.160	448	-0.004	0.048	0.002	0.136
J080801.74+330009.2	1.90	1.888	0.029	SMC	-0.032	151	0.001	0.044	-0.028	0.112
J081116.06+083837.7	2.07	1.906	0.081	SMC	-0.027	247	-0.003	0.049	-0.031	0.127
J081540.60+264021.6	1.94	1.681	0.109	LMC	0.364	428	-0.012	0.043	-0.027	0.142
J082003.40+155932.9	1.95	1.547	0.203	LMC2	0.420	373	-0.004	0.069	-0.012	0.142
J085206.65+193548.4	1.91	1.788	0.050	SMC	0.032	580	-0.003	0.044	-0.020	0.112
J085437.60+031734.8	2.24	1.567	0.070	SMC	0.263	192	-0.003	0.054	0.050	0.106
J085726.79+185524.3	1.89	1.730	0.016	SMC	0.063	81	-0.004	0.053	-0.064	0.107
J090558.75+553039.2	1.57	1.579	-0.019	SMC	0.070	692	-0.002	0.041	0.011	0.080
J090942.56+532126.5	2.07	1.628	0.003	SMC	0.003	527	-0.005	0.044	-0.019	0.140
J091516.27+071750.9	2.38	1.681	-0.010	SMC	0.117	40	-0.017	0.077	0.019	0.206
J091721.37+015448.1	2.18	2.107	0.121	SMC	0.227	86	-0.014	0.031	0.006	0.114
J092759.79+154321.8	1.81	1.731	0.217	LMC2	0.331	357	-0.008	0.059	-0.018	0.092
J094529.37+552525.7	2.24	1.867	0.120	SMC	0.015	314	-0.006	0.043	-0.016	0.130
J095114.97+545736.5	1.80	1.613	-0.004	SMC	-0.027	397	-0.004	0.042	-0.015	0.109
J101544.34+310617.2	1.56	1.596	0.016	SMC	-0.006	685	0.000	0.043	0.012	0.085
J104705.76+205734.5	2.01	1.775	0.159	LMC2	0.277	282	-0.021	0.055	-0.036	0.133
J105436.96+542343.7	1.50	1.513	0.014	SMC	-0.008	319	0.001	0.037	0.007	0.072
J105746.42+662250.5	2.34	2.088	0.040	SMC	0.112	277	-0.010	0.037	-0.046	0.120
J111756.53+143716.9	2.09	2.001	0.049	SMC	0.085	560	-0.005	0.036	-0.030	0.097
J112250.95+143732.5	2.05	1.554	-0.028	SMC	0.032	106	0.003	0.047	-0.026	0.138
J112913.29-023740.9	1.86	1.623	0.020	SMC	-0.151	603	-0.003	0.045	-0.026	0.124
J113341.29-005740.1	1.68	1.706	0.266	SMC	0.062	386	-0.002	0.042	0.002	0.094
J114141.84+444206.1	1.96	1.903	0.149	LMC2	0.368	398	-0.023	0.060	-0.028	0.109
J115153.87+150945.0	3.05	2.400	-0.007	SMC	0.110	92	-0.007	0.033	-0.105	0.176
J115705.51+615521.7	2.51	2.460	0.215	SMC	0.370	148	-0.014	0.033	-0.087	0.101
J120935.79+671715.7	2.03	1.843	0.094	MW	0.394	300	-0.013	0.028	-0.039	0.119
J122825.67+303038.6	3.91	3.098	-0.034	SMC	0.067	43	-0.008	0.061	0.412	0.471
J123714.61+064759.6	2.78	2.691	0.143	LMC2	0.431	35	-0.026	0.074	-0.168	0.156
J124708.43+500320.8	2.27	2.135	0.075	LMC	0.319	357	-0.012	0.029	-0.037	0.124
J124829.71+284858.1	1.54	1.513	-0.035	SMC	-0.049	1035	-0.002	0.041	0.022	0.092
J124841.45+302433.0	2.06	1.691	-0.025	SMC	-0.019	583	-0.004	0.042	-0.024	0.136
J125552.60+223424.4	1.82	1.526	0.036	SMC	0.141	898	-0.004	0.041	-0.015	0.134
J130225.28+211158.6	1.76	1.656	-0.004	SMC	-0.139	452	-0.012	0.036	-0.002	0.114
J130628.87+281550.8	2.10	2.012	0.078	SMC	0.015	465	-0.008	0.034	-0.030	0.099
J130828.43+584000.6	3.09	2.473	0.020	SMC	-0.158	54	-0.010	0.037	-0.144	0.211
J131129.11+222552.6	3.14	3.093	0.036	SMC	0.067	82	-0.011	0.036	-0.054	0.345
J131400.57+054319.5	1.89	1.583	0.046	SMC	0.270	340	-0.006	0.044	-0.013	0.120
J134122.51+185214.0	2.00	1.544	-0.016	SMC	0.000	32	0.003	0.053	-0.001	0.185
J134601.10+064408.4	2.09	1.512	0.015	SMC	0.034	118	-0.015	0.040	0.036	0.130
J135122.00+461828.5	1.81	1.606	0.142	LMC2	0.408	680	-0.005	0.067	-0.027	0.123
J141550.47+300146.9	2.08	1.676	0.074	SMC	0.226	83	-0.001	0.045	-0.033	0.245
J141606.79+180403.2	2.13	1.622	0.056	SMC	-0.027	108	-0.016	0.035	0.018	0.150
J143243.93+330746.7	2.09	2.058	0.010	SMC	-0.005	352	-0.003	0.041	-0.039	0.095
J143657.87+291100.6	1.77	1.596	0.147	LMC	0.514	812	-0.003	0.049	-0.014	0.111
J143912.05+111740.6	2.58	2.418	0.172	LMC2	0.271	52	-0.033	0.145	-0.080	0.098
J144929.27+333811.0	2.17	2.021	0.018	SMC	-0.157	89	-0.009	0.029	0.025	0.137
J145432.54+343523.9	1.61	1.580	0.293	LMC2	0.631	346	-0.002	0.058	-0.002	0.089
J145953.25+012944.2	1.66	1.623	0.157	LMC2	0.331	842	-0.006	0.057	0.011	0.089
J150738.73+415530.6	1.79	1.674	0.056	LMC	0.251	806	-0.005	0.040	-0.003	0.111
J152209.12+083020.0	1.93	1.627	0.017	SMC	-0.057	169	-0.016	0.035	-0.031	0.134
J160320.76+170117.8	1.99	1.890	-0.010	SMC	0.030	406	-0.004	0.043	-0.033	0.108
J160457.51+220300.5	1.98	1.641	0.263	LMC2	0.735	225	-0.007	0.075	-0.041	0.151
J161526.65+264813.8	2.18	2.118	0.035	SMC	0.120	324	-0.005	0.042	-0.037	0.095
J162321.43+135532.4	1.75	1.751	0.031	SMC	0.034	816	-0.005	0.036	0.006	0.093
J164610.20+232923.0	2.06	1.998	-0.027	SMC	-0.031	284	-0.004	0.043	-0.037	0.092
J170542.92+354340.4	2.01	2.038	0.146	LMC2	0.364	210	-0.009	0.075	-0.030	0.077
J212329.47-005053.0	2.26	2.060	-0.011	SMC	0.000	32	0.002	0.041	-0.023	0.123
J222910.16+141402.2	2.11	1.586	-0.024	SMC	0.026	538	-0.004	0.041	0.006	0.136
J225719.04-100104.7	2.08	1.836	0.045	SMC	0.177	192	-0.007	0.039	-0.040	0.129
J233133.05-090246.6	2.44	1.734	0.101	LMC	0.393	38	0.002	0.089	0.084	0.215
J233156.49-090802.0	2.66	2.143	0.136	SMC	0.234	46	-0.008	0.078	-0.015	0.104
J233633.81-105841.5	2.04	1.829	0.004	SMC	-0.103	484	-0.003	0.045	-0.026	0.123
J234023.67-005327.1	2.09	2.054	0.057	SMC	-0.023	34	-0.001	0.047	-0.071	0.113
J235057.87-005210.0	3.03	2.426	0.003	SMC	0.001	42	-0.013	0.067	-0.098	0.169

<sup>a</sup> C.S. = control sample.